Electronic Supplementary Material (ESI) for Materials Horizons.

Supplementary Information

Laser-Induced Locally Controllable Craze-Like Microstructures for Polymer White Structural Coloration

*Jin Feng, Rui Xu, Jiameng Huang, and Tao Zhou**

State Key Laboratory of Polymer Materials Engineering of China, Polymer Research Institute, Sichuan University, Chengdu 610065, China

*Corresponding authors. E-mail address: zhoutaopoly@scu.edu.cn (T. Zhou)

1. Experimental Section

1.1. Materials

CuNWs (99.5%) were purchased from Xuzhou Jiechuang Materials Co., Ltd. (China). LDPE and POM were provided by Shenhua Chemical Company (China). EMA-GMA terpolymer was supplied by Arkema Co. (French). PR was bought from Shanghai Jingyan Chemical Company (China). PP (1120, melt flow rate = 15 g/10 min) was purchased from Formosa Plastics Industrial (Ningbo) Co., Ltd. All materials in this study were freshly used without further treatment.

1.2. Preparation of the Core-Shell Microfibers

In our work, the core-shell microfibers with CuNWs as core and POM as shell were in-situ constructed by melt blending in-situ fibrillation. Firstly, the homogeneously mixed CuNWs (2.5 g) and POM (497.5 g) were blended by an extruder (Φ20) at 210 °C, and the screw speed was 120 rpm. Then, the first melt blending product (300 g), EMA-GMA (25 g), and LDPE (175 g) were mixed by an extruder (temperature: 220 °C; screw speed: 240 rpm). Herein, the second melt blending process was a critical step because the CuNWs@POM core-shell microfibers were formed by the in situ fibrillation under the shearing and stretching effect. In the second melt blending, the use of EMA-GMA (compatibilizers) is necessary because it would accelerate the microfibers' formation in the LDPE matrix. EMA-GMA is a random terpolymer composed of repeat units of ethylene, methyl acrylate, and glycidyl methacrylate (GMA). This terpolymer is used as a reactive compatibilizer because of its reactive repeating unit of GMA on the backbone. The GMA repeating unit contains the reactive epoxy group, which has high reactivity with −OH, −COOH, $-NH_2$, and so on. In general, the POM macromolecular chains usually contain terminal hydroxyls (−OH). Therefore, the epoxy groups on the GMA repeating units can react with the terminal hydroxyl groups of POM. Moreover, LDPE is one of the most common nonpolar polymers. The ethylene repeating units of EMA-GMA possess excellent physical compatibility with LDPE. Thus, the EMA-GMA can boost the construction of CuNWs@POM microfibers in the nonpolar polymer matrix (LDPE) during the second melt blending process.

1.3. Fabrication of Polymer Plates for white structural color

After drying, the final blended product containing core-shell microfibers was added to the polymers. Firstly, the final composite product, PR, and PP were mixed, and the amount of the final composite product and PR was 7 wt % and 0.05 wt% by weight of PP, respectively. PP/CuNWs@POM/ PR were then blended by extrusion at 190 °C. Finally, the red PP plates (80.0 mm × 65.0 mm × 3.5 mm) were fabricated by injection molding at 200 °C. In addition, PP plates incorporated with neat CuNWs and PR were also prepared by the above method. To ensure that the contents of the laser absorber (CuNWs) and PR were consistent with the above samples, the amount of neat CuNWs and PR were 0.021 wt% and 0.05 wt % by weight of PP, respectively.

1.4. Preparation of polymer white structural color by LDW

Polymer white structural color was obtained by LDW on a NIR pulsed fiber laser (MF-E-A, λ=1064 nm) with total laser power and laser spot size of 20 W and 25 μm, respectively. The NIR laser scanning position and speed can be accurately controlled since an intelligent control board and galvanometer are used for the laser system. The texts or patterns designed by the software (EZCAD 2.0) can be precisely written on the surface of the polymer. In this experiment, we designed a vector graph with a coordinate system through EZCAD2.0 to seek out the optimal LDW parameters. The vector image was composed of 25 square patterns (10×10 mm^2). The vertical axis of the vector graph is the laser power (10-18 W), and the horizontal axis is the laser pulse frequency (20-100 kHz). In addition, the UV laser irradiation of polymers was performed on a 355 nm UV pulse fiber laser system (MUV-E-A) with total laser power and laser spot size of 5 W and 20 μm, respectively. And the 1064 nm NIR and 355 nm UV laser scanning speeds were both set at 1000 mm/s. In order to make the focus of the NIR and UV laser spots fall precisely on the polymer surface, we adjusted the distance from the focusing lens to the surface of the polymers.

1.5. Characterizations

X-ray diffraction (XRD) spectrum was recorded on a DX-1000 X-ray diffractometer (Rigaku). UV-Vis-NIR spectra were collected on a UV-3600 spectrometer (Shimadzu). It is worth noting that the reflectance spectra were measured by the integrating sphere method. The polymer plates were placed in the sample window of the integrating sphere, which collected all the diffuse reflection light and focused it on the detector. Finally, the signal difference between the sample and the reference sample ($BaSO_4$ standard white plate) was converted into the visible diffuse reflectance spectrum of the sample. Emissivity spectra were collected in the MIR range (2.5-15 μm) using an FTIR spectrometer (Nicolet iS50, ThermoFisher, USA) equipped with a diffuse gold integrating sphere (Pike Technologies, USA). X-ray photoelectron spectroscopy (XPS) was determined on a XASAM800 X-ray photoelectron spectrometer (Kratos) equipped with a monochromatic Al Kα achromatic X-ray source (1486.6 eV). Scanning electron microscopy (SEM) with energy dispersive spectrometry (EDS) was conducted by a field-emission scanning electron microscope (JEOL JSM-7500F). To obtain accurate cross-sectional morphology of samples, in our experiments, the SEM cross-sectional samples were prepared by brittle fracture in liquid nitrogen. The samples were placed in liquid nitrogen and fully immersed in liquid nitrogen for 3 min. Then, the samples were removed and immediately subjected to brittle fracture. The surface color measurements were conducted on a colorimeter (Konica Minolta CM-5). The degree of whiteness of the sample was measured by an automatic whiteness meter (WSD-3). Optical microscope (OM) images were captured on a digital microscope (Keyence VHX-1000C). Thermogravimetric analysis (TGA) curves were recorded on a thermogravimetric analyzer (NETZSCH TG 209F1). TGA-FTIR-GC-MS test was carried out on a TGA 8000 connected with FTIR Spectrum 3 and GCMS Clarus 690/SQ8T (Perkin Elmer). The temperature measurements were performed with an infrared thermal imaging camera (FLIR ONE PRO). All contact angle (CA) measurements were conducted on a contact-angle machine (Krüss K100). Laser scanning confocal microscopy (LSCM) images were taken on a laser scanning confocal microscope (LSM710CarlZeiss). Attenuated total reflection Fourier

Transform Infrared (ATR-FTIR) spectra were collected on an infrared spectrometer (Nicolet iS50) with a smart iTR accessory (Ge crystal). Micro-Raman spectra, Raman surface Imaging, and Raman depth Imaging were conducted on a micro-Raman spectrometer (Thermo Fisher Scientific DXRxi).

The mechanical properties of samples were tested under ambient conditions on a versatile testing machine (Instron-5567, USA) equipped with a sensor of 10 kN. Specifically, the tensile experiments were conducted at a stretching velocity of 50 mm/min using the dumbbell-shaped specimens (gauge length×width×thickness: 80 mm×10 mm×4 mm). Flexural experiments were tested at a speed of 2 mm/min using 3-point bending mode and the span length of 64 mm. The thickness, width, and length of flexural specimens were 4 mm, 10 mm, and 80 mm, respectively. In addition, a white structural color pattern (60 mm×10 mm) was prepared on the PP/PR/CuNWs@POM microfibers composites by LDW for the following mechanical properties tests. Note that each sample was tested 5 times, and the average value was calculated to obtain the mechanical properties of the samples.

For the adhesion test**,** according to the ASTM D3359, a multi-blade cutter with a tooth spacing of 2 mm was kept vertical to the plane of the tested sample and used to cut the white color layer at a speed of 30 mm/s. Then, the sample was rotated 90°, and the same cutting process was repeated to form a grid lattice graphic. After the required cuts, a soft brush was used to remove the detached flakes. Subsequently, a scotch tape (600-1PK, 3M) was placed on the grid with sound and even contact between the tape and the polymer surface. After 90 s, the scotch tape was removed by grasping the free end and quickly backing away from it at an angle as close to 180°. There are five levels defined in this standard, including grade 0B (the peeling area >65%), 1B (5-65%), 2B (15-35%), 3B (5-15%), 4B (0-5%), and 5B (the peeling area is 0%, without any peeling).

2. Supporting Figures and Tables

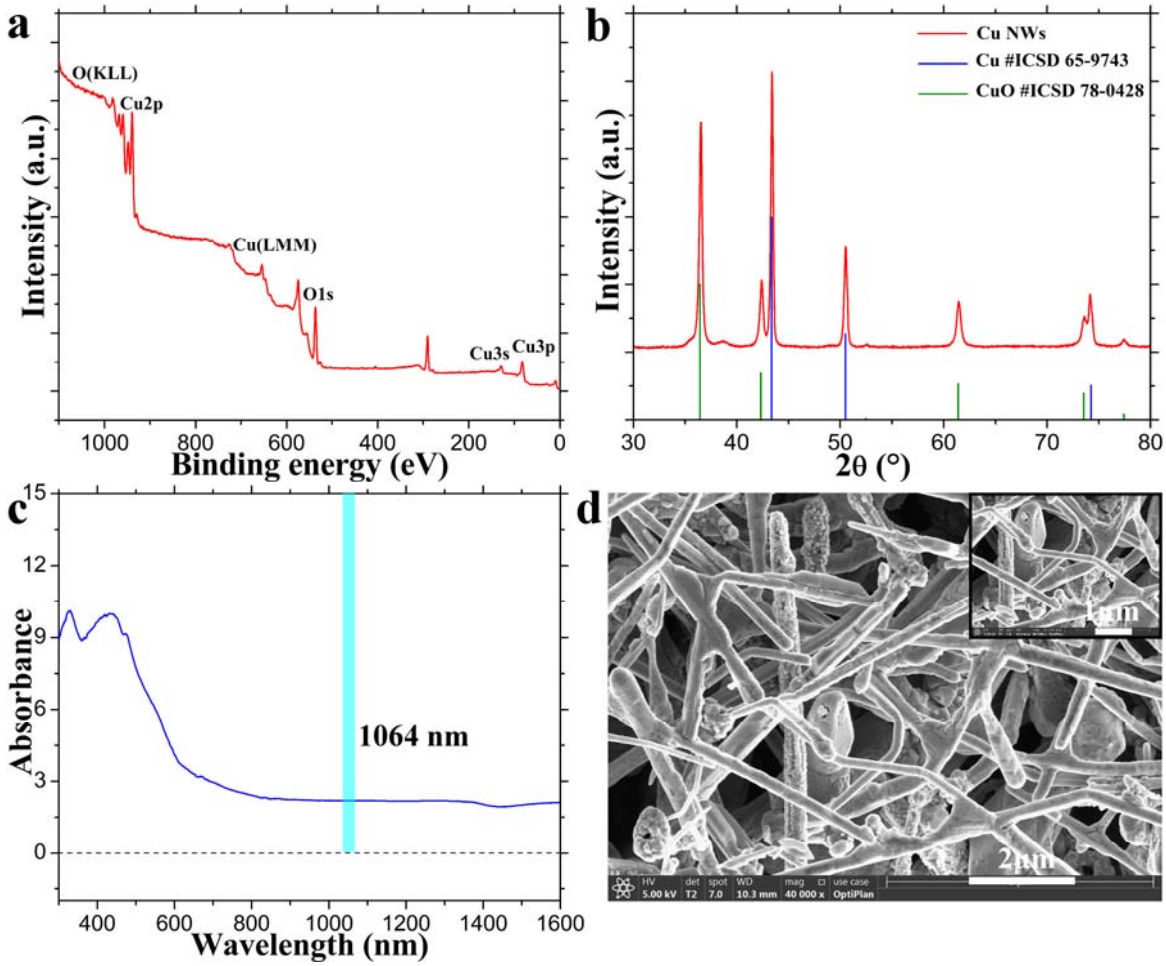

Figure S1. Spectroscopy and morphology characterizations of CuNWs. (a) XPS spectrum of CuNWs. **(b)** WAXD pattern of CuNWs (red) and standard patterns of Cu (blue) and CuO (green); **(c)** UV-Vis-NIR spectrum of CuNWs within 300−1600 nm; **(d)** SEM images of CuNWs.

Figure S1 shows the spectroscopy and morphology characterizations of CuNWs. The XPS spectrum presents the elements of Cu in CuNWs (**Figure S1**a). From the WAXD patterns of CuNWs, besides the standard diffraction peaks of Cu,[1] the diffraction peaks of the CuO are also observed,[2] indicating that some CuNWs have been partially oxidized to CuO (**Figure S1**b). In **Figure S1**c, CuNWs show a strong absorption at 1064 nm. In addition, it can be observed that the CuNWs are fibrous with different lengths and an average diameter of 120-150 nm (**Figure S1**d).

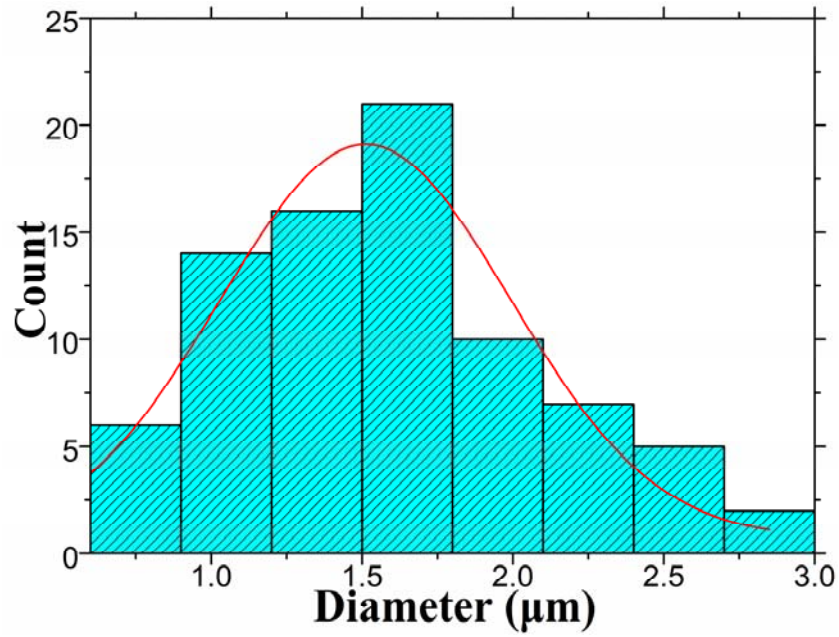

Figure S2. Diameter distribution of CuNWs@POM core-shell microfibers.

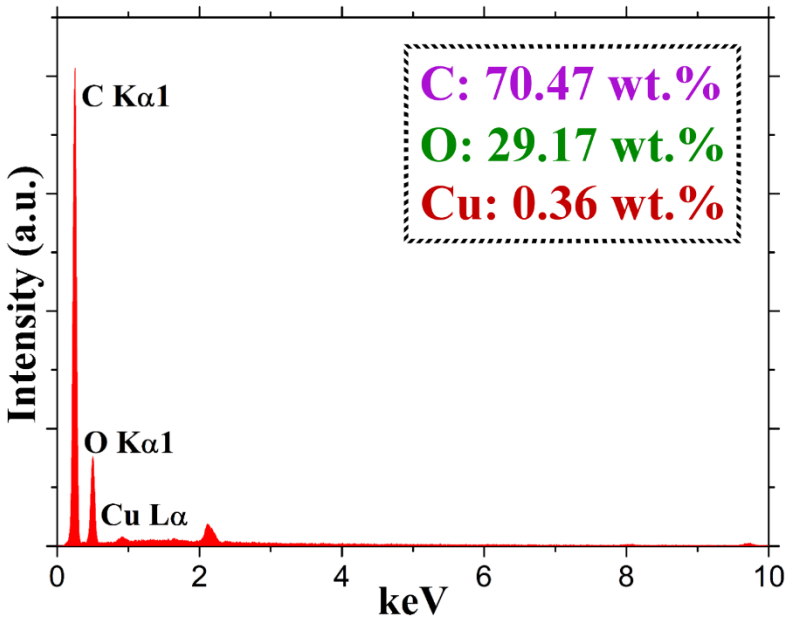

Figure S3. EDS spectrum of the cross-section of the individual CuNWs@POM core-shell microfiber.

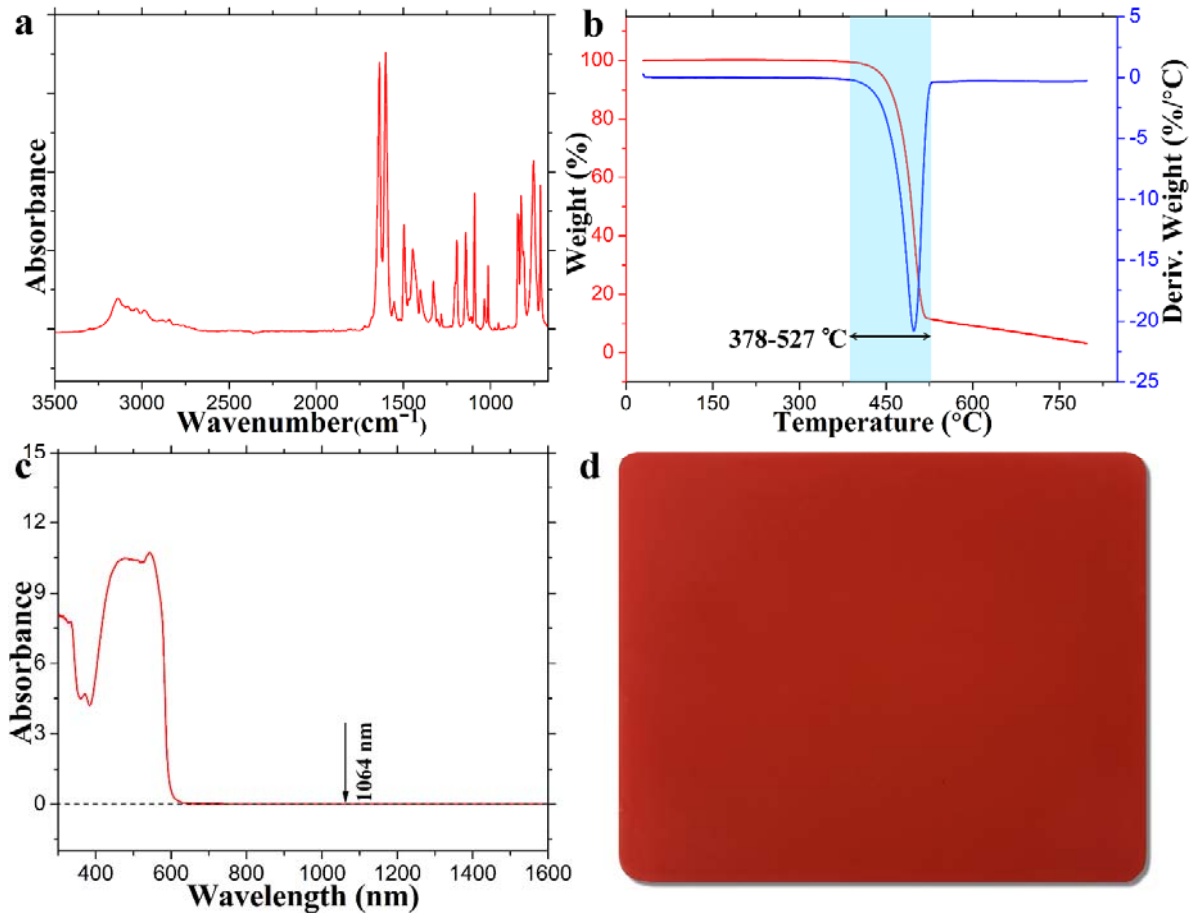

Figure S4. Spectroscopy characterizations of PR and photograph of PP doped with PR after LDW. (a) FTIR spectrum of PR; **(b)** TG and DTG curves of PR. The TG curve was measured at a heating rate of 10 °C/min between 30 °C and 800 °C in an air atmosphere. **(c)** UV-Vis-NIR spectrum of PR within 300−1600 nm (λ=1064 nm are located at the position of the arrow); **(d**) Digital photograph of PP doped with PR after NIR LDW.

Figure S4a and **Figure S4**b show the FTIR spectrum and TG curve of PR, respectively. The decomposition temperature of PR is from 378 °C to 527 °C. As shown in **Figure S4**c, PR has no absorption in the NIR region at 1064 nm. Therefore, it can be observed that there is no color change on the surface of PP doped with 0.05% PR after NIR LDW (**Figure S4**d).

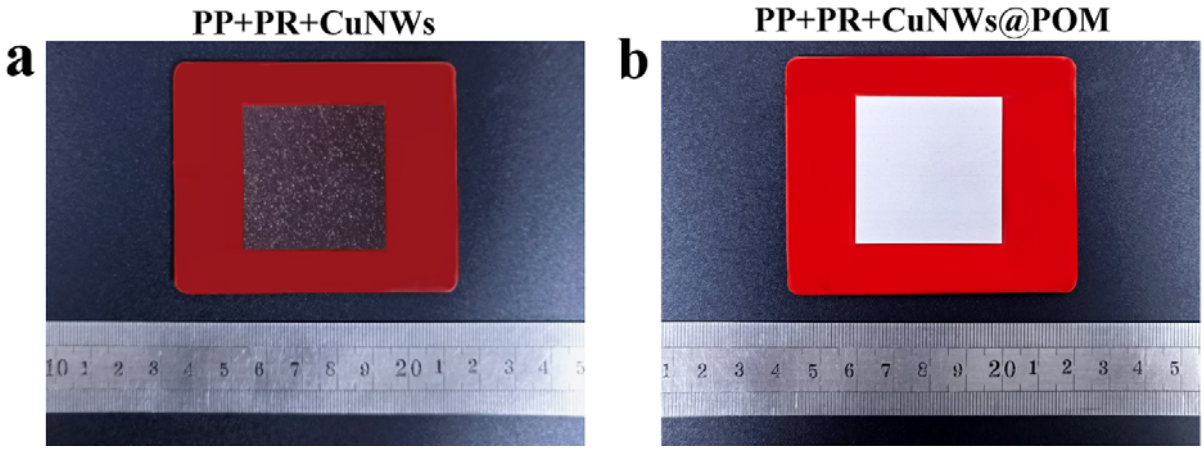

Figure S5. Digital photographs of PP doped with PR and CuNWs (a) and PP doped with PR and CuNWs@POM core-shell microfibers (b) after laser irradiation with larger square patterns (40 mm × 40 mm).

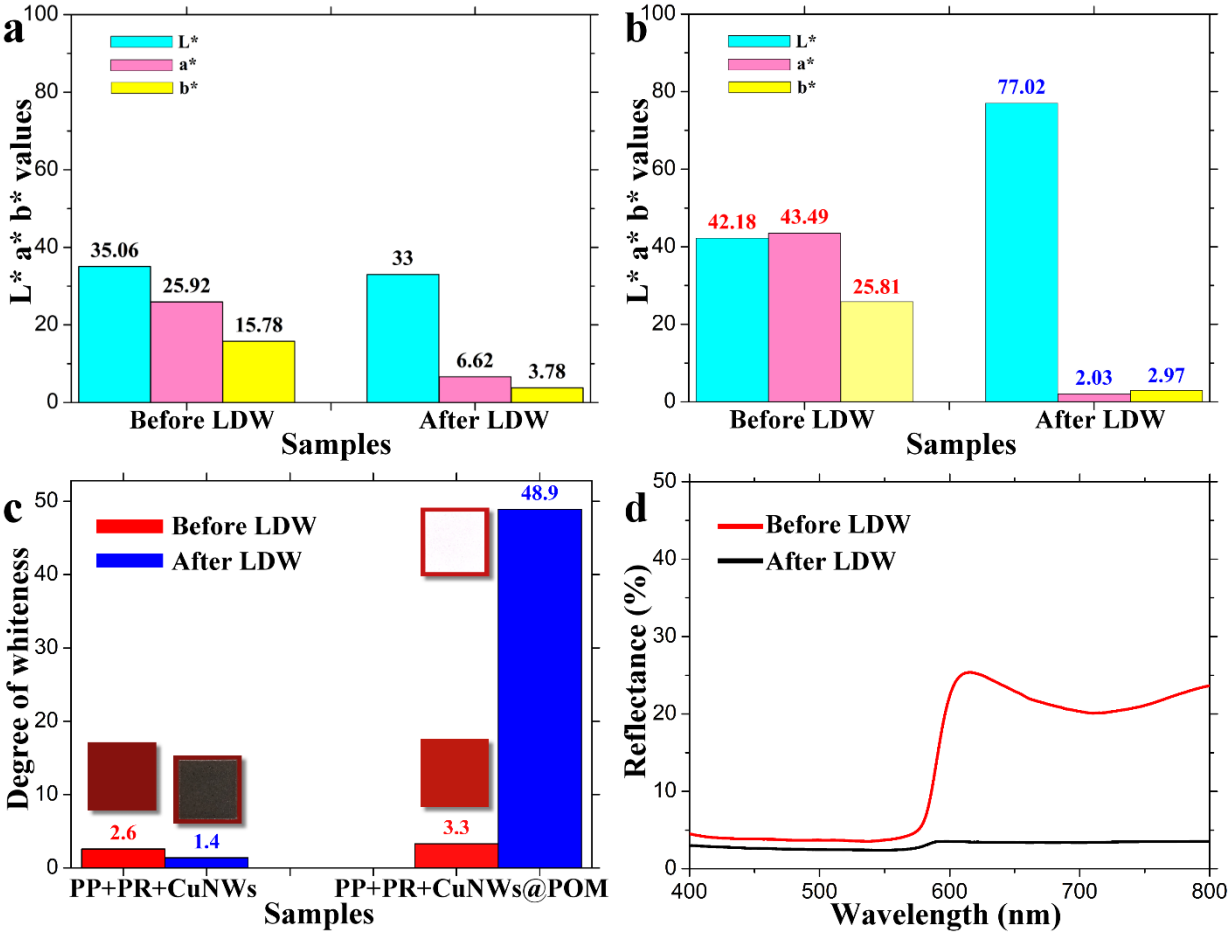

Figure S6. L*a*b* values, degree of whiteness, and reflectance of samples. (a) L*a*b* values of PP doped with PR and CuNWs before and after laser irradiation. **(b)** L*a*b* values of PP doped with PR and CuNWs@POM core-shell microfibers before and after laser irradiation. **(c)** Degree of whiteness for samples before and after LDW. The square patterns are the corresponding test samples. **(d)** Reflectance of PP doped with PR and CuNWs before and after laser irradiation.

Figure S6a and b are the L*a*b* values of PP doped with PR and CuNWs and PP doped with PR and CuNWs@POM core-shell microfibers before and after laser irradiation, respectively. Herein, the L*, a*, and b* represent the lightness, redness-greenness, and yellowness-blueness, respectively. As shown in **Figure S6**a, for PP doped with PR and CuNWs, the L* value decreases from 35.06 to 33, visually appearing darker after laser patterning. The a* value changes from 25.92 to 6.62, and the b* value changes from 15.78 to 3.78, demonstrating red-yellow fading. In **Figure S6**b, for PP doped with PR and CuNWs@POM core-shell microfibers, the L* value increases from 42.18 to 77.02, showing a remarkable increase in the brightness of the polymer

surface after laser direct writing microstructures. The a* value changes from 43.49 to 2.03, and the b* value changes from 25.81 to 2.97, illustrating a color change from red-yellow to white. Furthermore, according to "CIE 1931" standards, ΔE can be used to evaluate the color difference between the pristine and test samples. The color difference (ΔE) was calculated using the following equation:

$$\Delta E^* = \sqrt{(\Delta L^*)^2 + (\Delta a^*)^2 + (\Delta b^*)^2}$$

$$\Delta L^* = L^* - L_0$$

$$\Delta a^* = a^* - a_0$$

$$\Delta b^* = b^* - b_0$$

where L*, a*, and b* values are measured from the color change patterns after laser irradiation, L_0, a_0, and b_0 representing the measured values of the pristine sample before laser irradiation (red polymer plate), and ΔL*, Δa*, and Δb* are the differences between values of L*, a*, and b*.

Here, the color differences (ΔE) of PP doped with PR and CuNWs and PP doped with PR and CuNWs@POM core-shell microfibers before and after laser irradiation are calculated to be 22.81 and 58.77, respectively. The color difference between the white structural color and red is apparently greater than that between black and red. Therefore, the contrast of the white structural color pattern is significantly higher than the black pattern.

In addition, the degree of whiteness test was carried out to illustrate their difference further. An automatic whiteness meter (WSD-3, Beijing Kangguang Optical Instruments Co., Ltd.) was used to measure the degree of whiteness. The light source was a halogen lamp, and the diameter of the test hole was 15 mm. And the obtained degree of whiteness was blue-ray whiteness according to ISO 2470. As shown in **Figure S6**c, for PP doped with PR and CuNWs, the degree of whiteness is decreased from 2.6 to 1.4 after laser irradiation. In comparison, for PP doped with PR and CuNWs@POM core-shell microfibers, the degree of whiteness is increased from 3.3 to 48.9 after laser treatment. The degree of whiteness results again manifest the apparent

difference of color change between the white coloration and traditional laser patterning. Moreover, the reflectance of PP doped with PR and CuNWs after laser patterning shows an overall decline from 400 nm to 800 nm (especially within the range of red light from 620 nm to 800 nm) due to the generation of black color (**Figure S6**d).

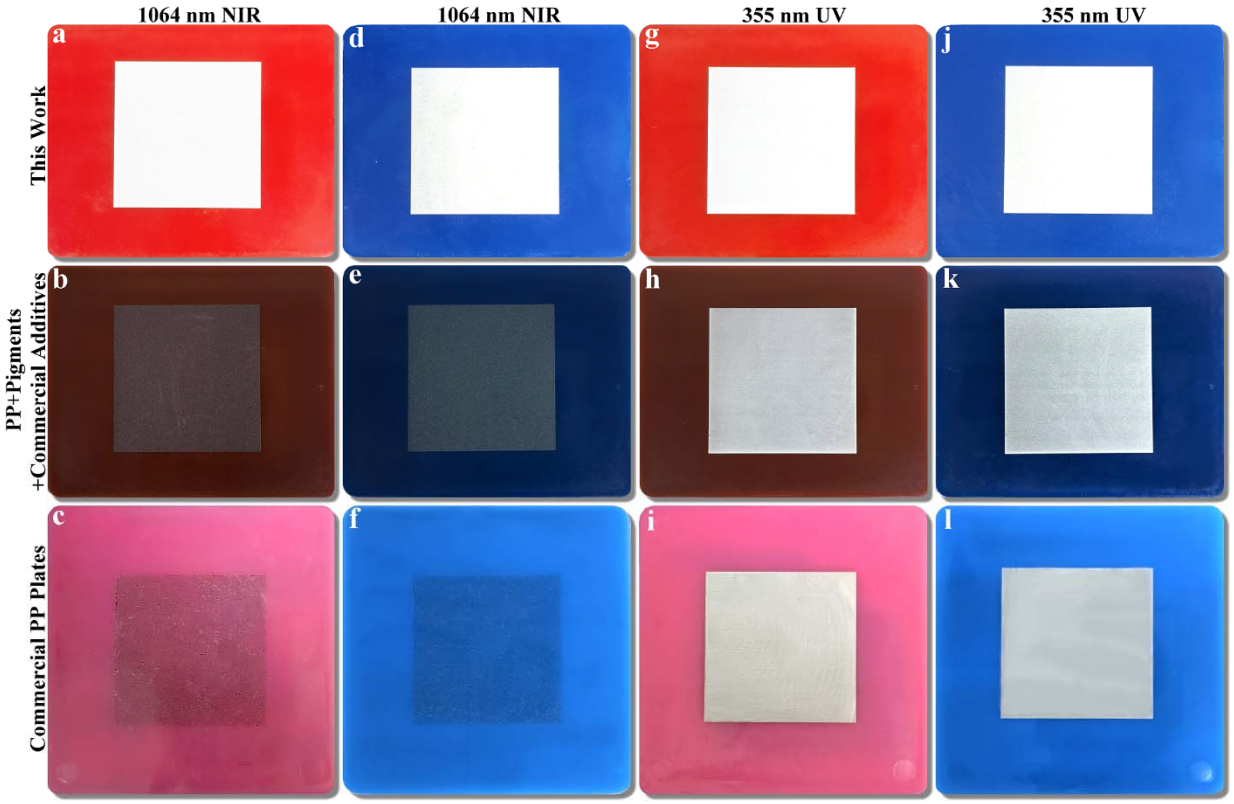

Figure S7. Digital photographs of comparisons between the laser direct writing white structural color and conventional laser marking. Photographs of the PP doped with different pigments and CuNWs@POM core-shell microfibers after **(a, d)** 1064 nm NIR laser direct writing and **(g, j)** 355 nm UV laser direct writing. Photographs of the PP doped with different pigments and commercial additives after **(b, e)** 1064 nm NIR laser marking and **(h, k)** 355 nm UV laser marking. Photographs of the colored laser-markable commercial PP plates after **(c, f)** 1064 nm NIR laser marking and **(i, l)** 355 nm UV laser marking, and these plates were directly purchased.

To compare laser direct writing white structural color with conventional white laser marking, we purchased commercially available white laser marking additives and colored laser-markable commercial PP plates for white laser marking. The white laser marking additives are composed of carbon materials and metal oxide absorbers. The colored laser-markable commercial PP plates can be laser-marked directly. The suppliers of these two materials informed us in advance that only UV lasers can be used to produce the white mark on colored plastics, and using NIR lasers would lead to failure. Moreover, none of these two suppliers currently have products suitable for white laser marking on colored plastics using NIR lasers, and they also confirmed that there are currently no products on the market that can work for NIR lasers. Then we prepared PP doped with 0.05 wt% pigments (red and blue) and 7 wt% CuNWs@POM core-shell microfibers and

PP doped with 0.05 wt% pigments (red and blue) and 4 wt% commercial white laser marking additives. Herein, the NIR laser irradiation of polymers was conducted on 1064 nm NIR pulse fiber laser system (MF-E-A), and UV laser irradiation of polymers was carried out on 355 nm UV pulse fiber laser system (MUV-E-A). The parameters of the NIR laser were 16 W, 60 kHz, and 1000 mm/s, and those of the UV laser were 4 W, 30 kHz, and 1000 mm/s. The patterns of 40 mm×40 mm were prepared on the colored PP plates.

Figure S7a-f shows the digital photographs of the samples after 1064 nm NIR laser irradiation. As shown in **Figure S7**a, d, the bright and high-contrast white color patterns are precisely prepared on the PP doped with pigments and CuNWs@POM core-shell microfibers (this work) after 1064 nm NIR laser irradiation. In **Figure S7**b, e, dark gray patterns are observed on the PP doped with pigments and commercial additives after NIR laser irradiation. The extremely blurry shallow black color patterns are generated on the colored laser-markable commercial PP plates after NIR laser irradiation (**Figure S7**c, f), just as the supplier told us in advance. **Figure S7**g-l presents the digital photographs of the samples after 355 nm UV laser irradiation. Surprisingly, in **Figure S7**g, j, PP doped with pigments and CuNWs@POM core-shell microfibers also exhibit a bright white color after 355 nm UV LDW. As shown in **Figure S7**h, k and **Figure S7**i, l, after 355 nm UV laser irradiation, white patterns are observed on PP doped with pigments and additives and the colored laser-markable commercial PP plates. Obviously, the white coloration effect (brightness and contrast) of NIR and UV laser direct writing in this study are both significantly better than that of conventional UV white laser marking (commercial products).

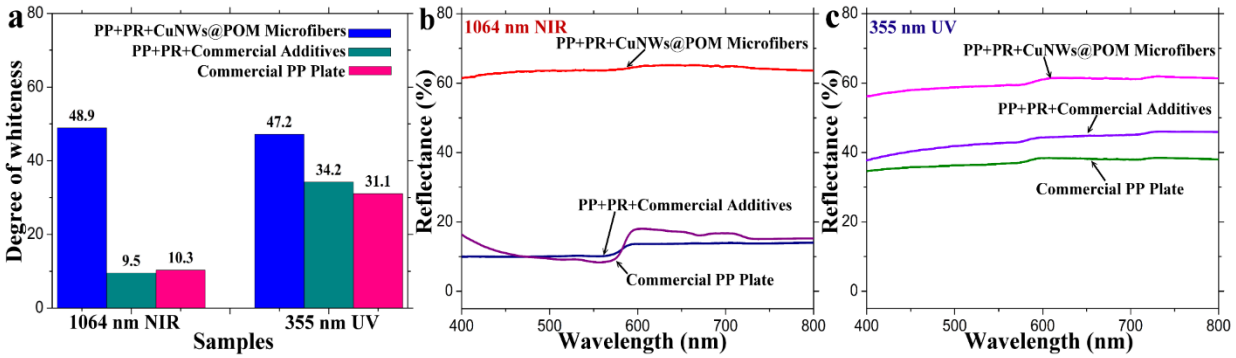

Figure S8. Whiteness and reflectance of samples in Figure S7a-c (NIR laser) and Figure S7g-i (UV laser). (a) Whiteness of samples after 1064 nm NIR and 355 nm UV laser irradiation. **(b)** Reflectance of samples after 1064 nm NIR laser irradiation. **(c)** Reflectance of samples after 355 nm UV laser irradiation.

The whiteness and reflectance measurements were carried out to demonstrate the difference between this work and conventional white laser marking. Herein, the patterns (40 mm×40 mm) in **Figure S7**b, c, and **Figure S7**g-i were chosen for the following characterizations. As shown in **Figure S8**a, for PP doped with PR and CuNWs@POM core-shell microfibers, the degrees of whiteness are 48.9 and 47.2 after 1064 nm NIR and 355 nm UV laser direct writing, respectively. In comparison, for PP doped with PR and commercial additives and the red laser-markable commercial PP plate, the degrees of whiteness are 34.2 and 31.1 after 355 nm UV laser irradiation, respectively. The whiteness of the white patterns prepared by 1064 nm NIR and 355 nm UV laser direct writing in this work is much higher than those fabricated by conventional 355 nm UV white laser marking (commercial products). Moreover, the reflectance results again show the apparent difference in white color change between the laser direct writing white structural color and commercial white laser marking. The reflectance of the white patterns prepared in this work by 1064 nm NIR and 355 nm UV laser direct writing is also obviously higher than those of the white patterns fabricated by commercial 355 nm UV white laser marking (**Figure S8**b, c).

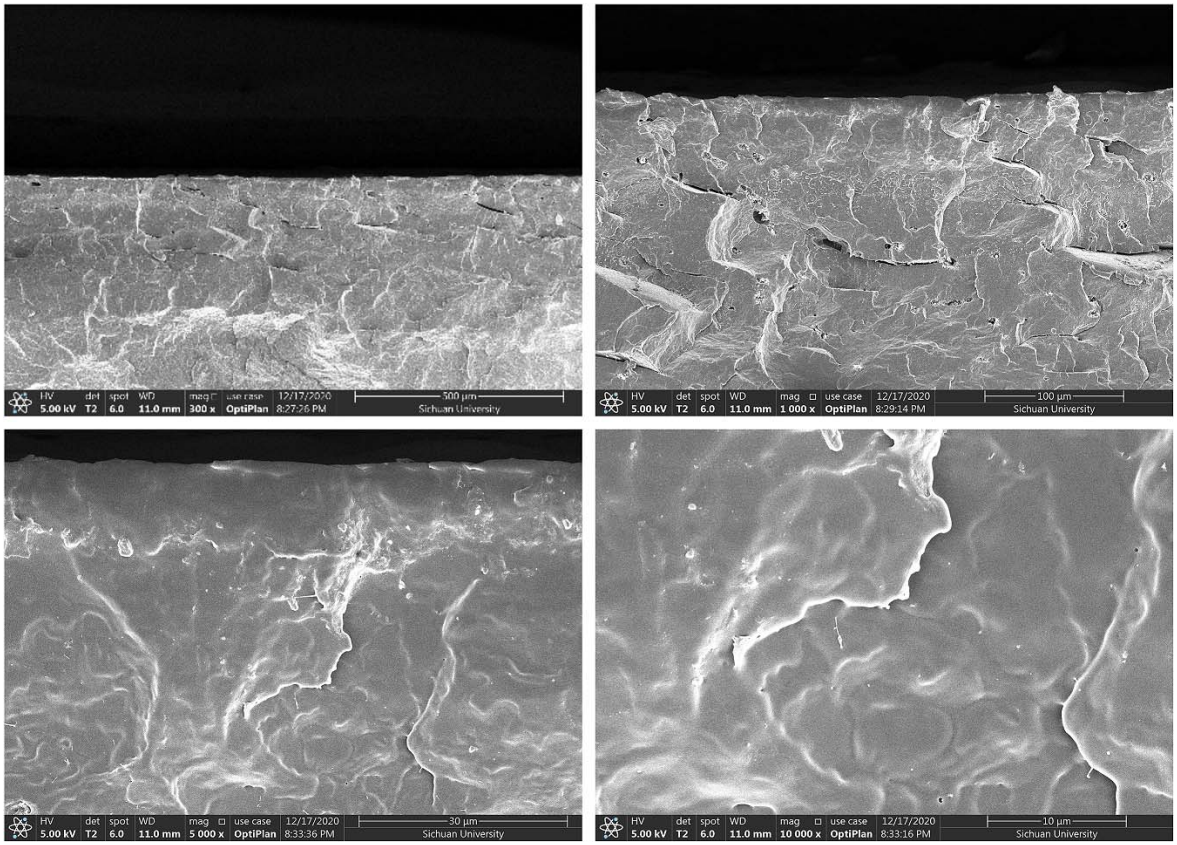

Figure S9. Cross-sectional SEM images of the neat PP after LDW with different magnifications.

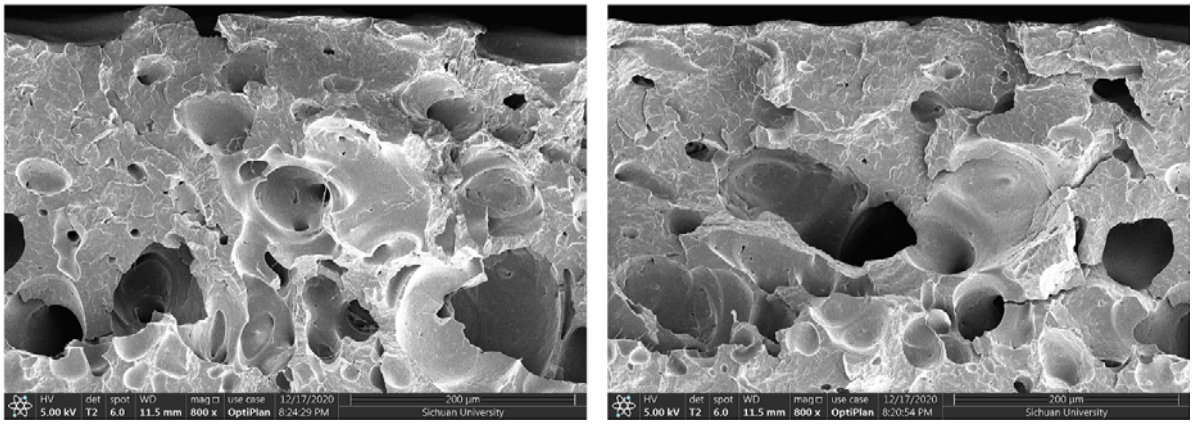

Figure S10. Cross-sectional SEM images of the PP doped with PR and CuNWs after LDW with a magnification of ×800.

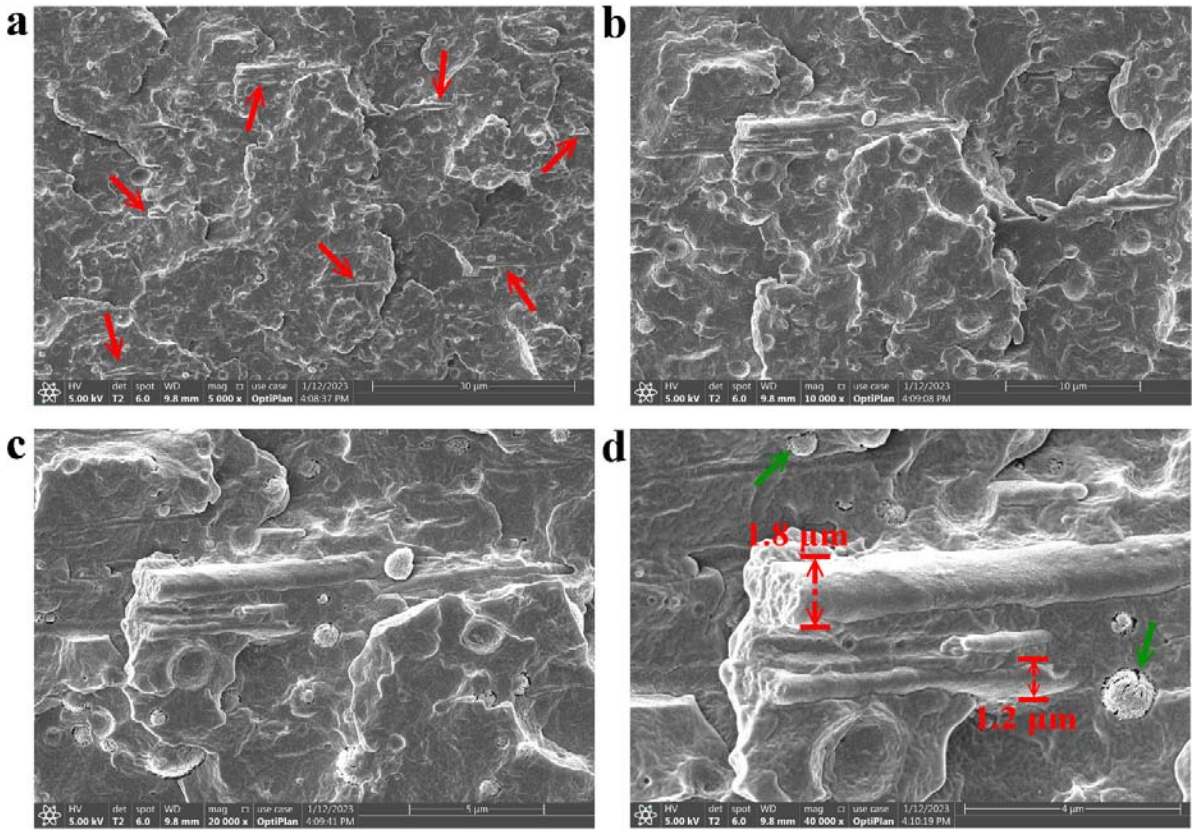

Figure S11. Cross-sectional SEM images of the PP doped with PR and CuNWs@POM core-shell microfibers before NIR LDW with different magnifications.

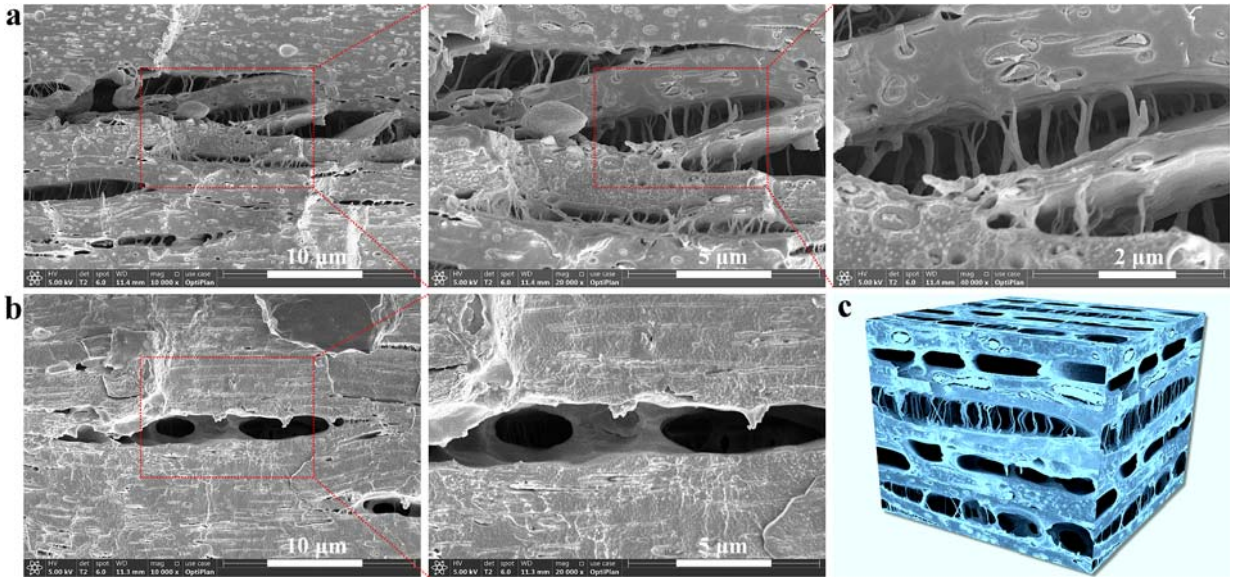

Figure S12. SEM images of craze-like microstructures. (a, b) SEM images of craze-like microstructures with different magnifications. **(c)** Schematic illustration of the mechanism of the craze-like microstructures induced by NIR LDW.

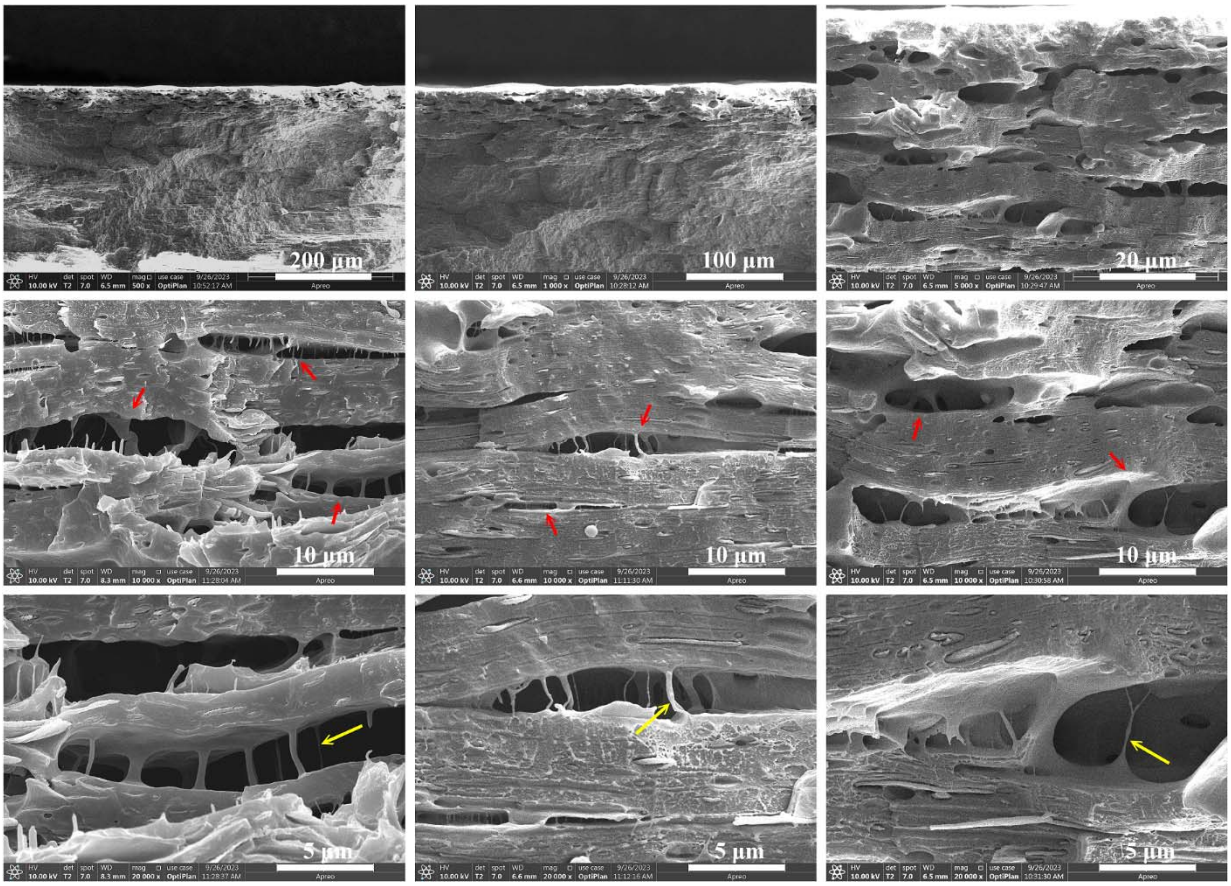

Figure S13. Cross-sectional SEM images of the white structural color pattern on PP doped with PR and CuNWs@POM core-shell microfibers after 355 nm UV laser direct writing with different magnifications.

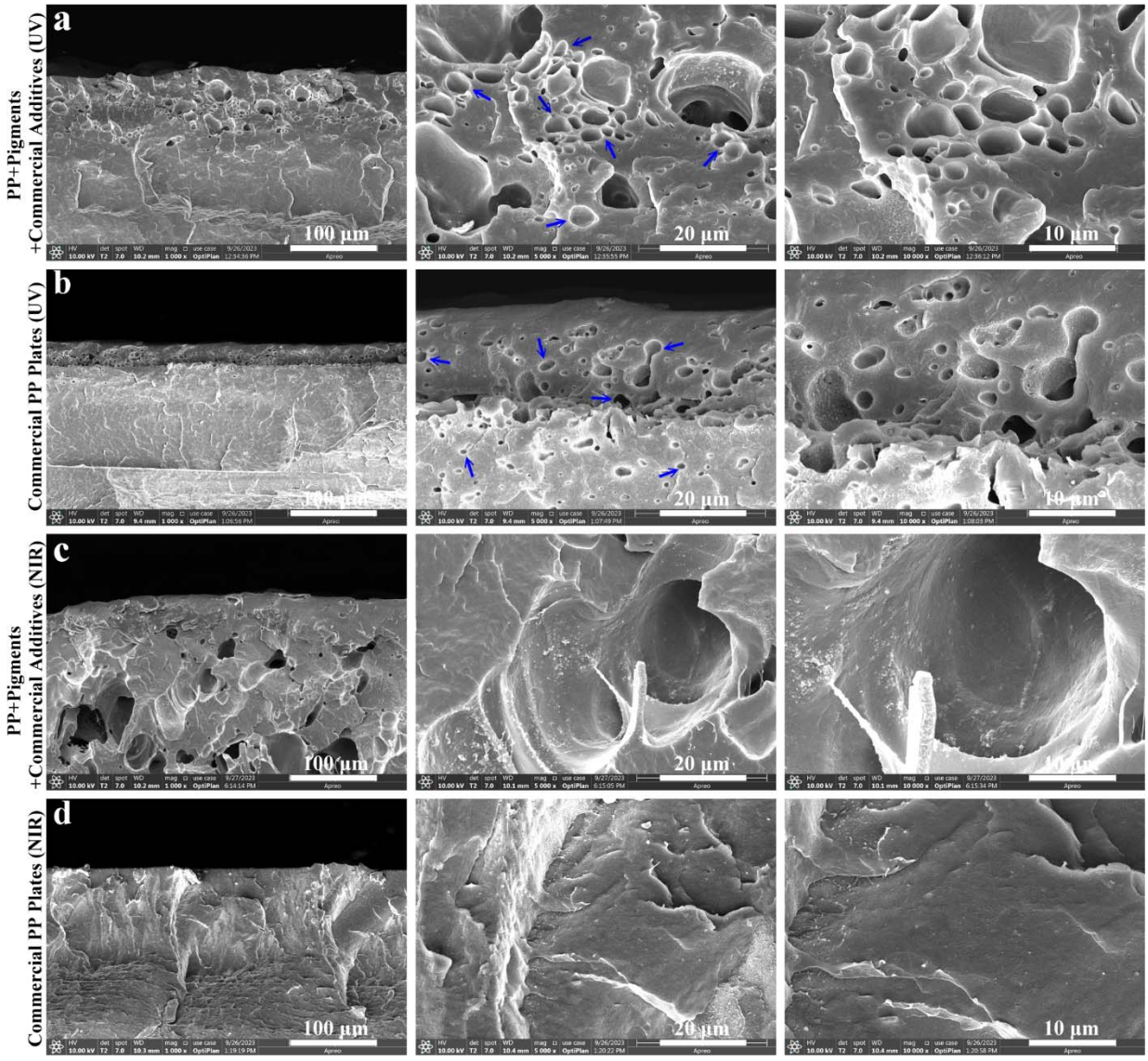

Figure S14. Cross-sectional SEM images of the patterns prepared by conventional laser marking with different magnifications. (a) The PP doped with PR and commercial additives after 355 nm UV laser marking. **(b)** The red laser-markable commercial PP plate after 355 nm UV laser marking. **(c)** The PP doped with PR and commercial additives after 1064 nm NIR laser marking. **(d)** The red laser-markable commercial PP plate after 1064 nm NIR laser marking.

For PP doped with PR and commercial additives and the red laser-markable commercial PP plate, many cell structures are formed in the laser-irradiated area after 355 nm UV laser irradiation (**Figure S14**a, b). These cell structures are circular with different sizes. This result fully confirms that the white colors produced by conventional UV white laser marking are ascribed to the generation of traditional cell structures, completely different from the craze-like microstructures generated by NIR and UV laser direct writing. However, many irregularly

broken voids are produced in the cross-section of PP doped with PR and commercial additives after NIR laser irradiation (**Figure S14**c), resulting in a dark gray color. As shown in **Figure S14**d, no microstructure is observed in the cross-section of the red laser-markable commercial PP plate after NIR laser irradiation.

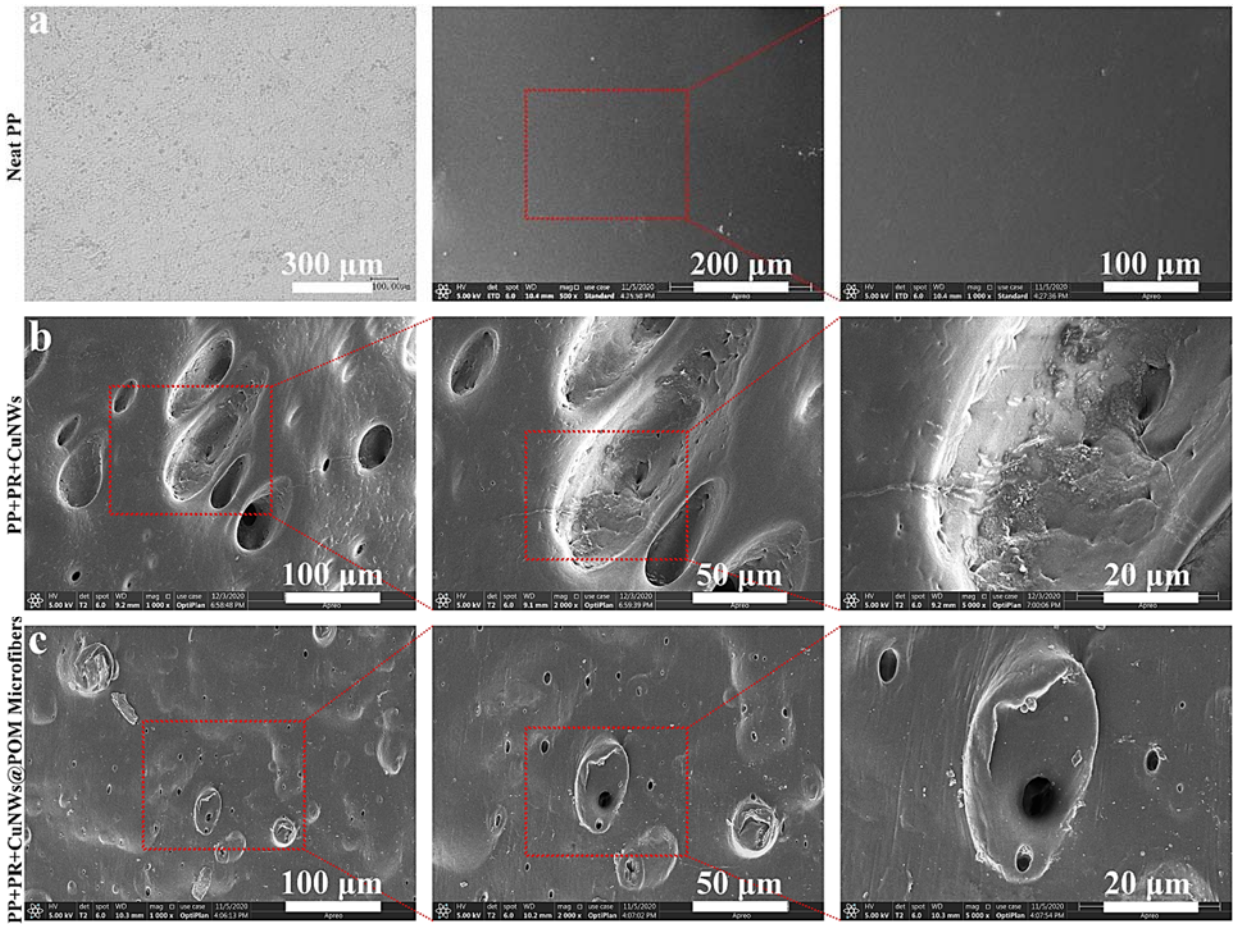

Figure S15. Surface morphology of samples after LDW. (a) Surface OM image and SEM images of neat PP after NIR LDW. **(b)** surface SEM images of the black pattern on PP doped with PR and CuNWs after LDW with different magnifications. **(c)** surface SEM images of the white pattern on PP doped with PR and CuNWs@POM core-shell microfibers after LDW with different magnifications.

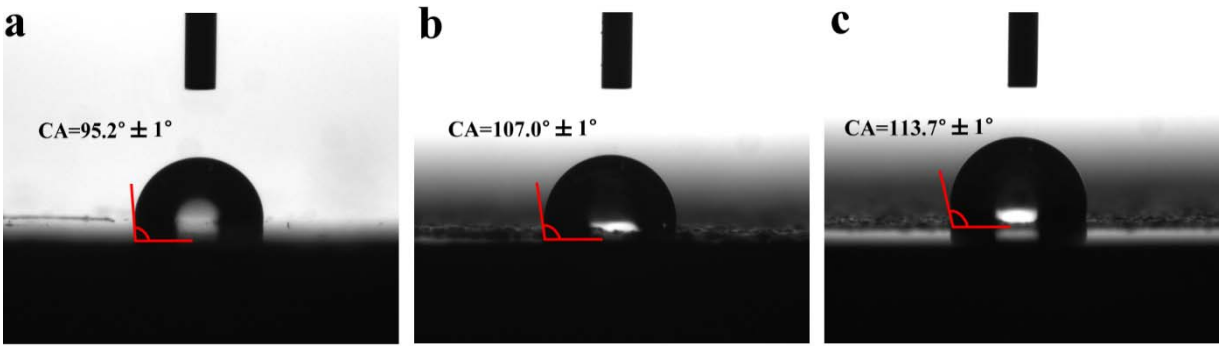

Figure S16. Surface contact angles of neat PP (a), PP doped with PR and CuNWs (b), and PP doped with PR and CuNWs@POM core-shell microfibers (c) after NIR LDW.

The surface CA of the samples is enhanced owing to the generation of rough morphology. The CAs of neat pp, PP doped with PR and CuNWs, and PP doped with PR and CuNWs@POM core-shell microfibers are 95.2°, 107°, and 113.7°, respectively. The CA of PP doped with PR and CuNWs@POM core-shell microfibers is lower than that of PP doped with PR and CuNWs because it has a relatively flat and uniform surface morphology.

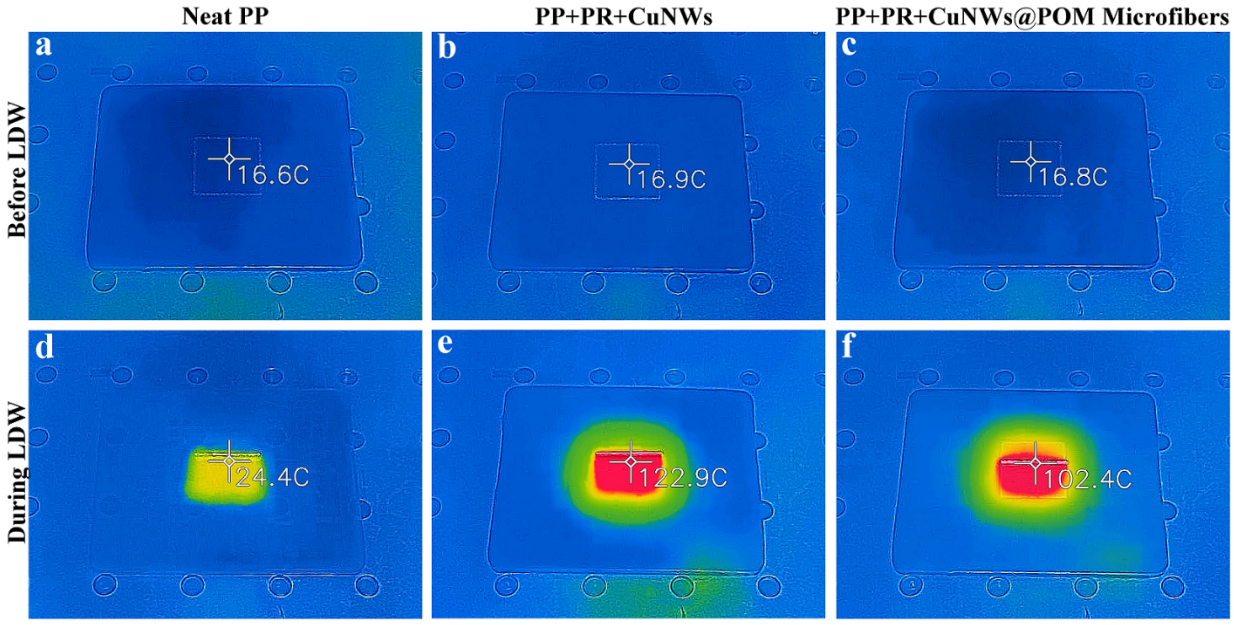

Figure S17. Infrared thermal images of neat PP (a, d), PP doped with PR and CuNWs (b, e), and PP doped with PR and CuNWs@POM core-shell microfibers (c, f) before and after NIR LDW.

Except for neat PP, the surface temperatures during LDW are obviously higher than before LDW, demonstrating that the photothermal effect is very significant. It should be noted that the temperatures are just recorded on the polymer surface by infrared thermal imaging, not the instantaneous high temperature at the NIR laser focus spot inside the polymer matrix during laser irradiation. In our previous study,[3,4] the instantaneous temperature calculated at the focus position of the NIR laser is up to 700 °C, which is high enough to cause the thermal decomposition of the POM, PP, and PR.

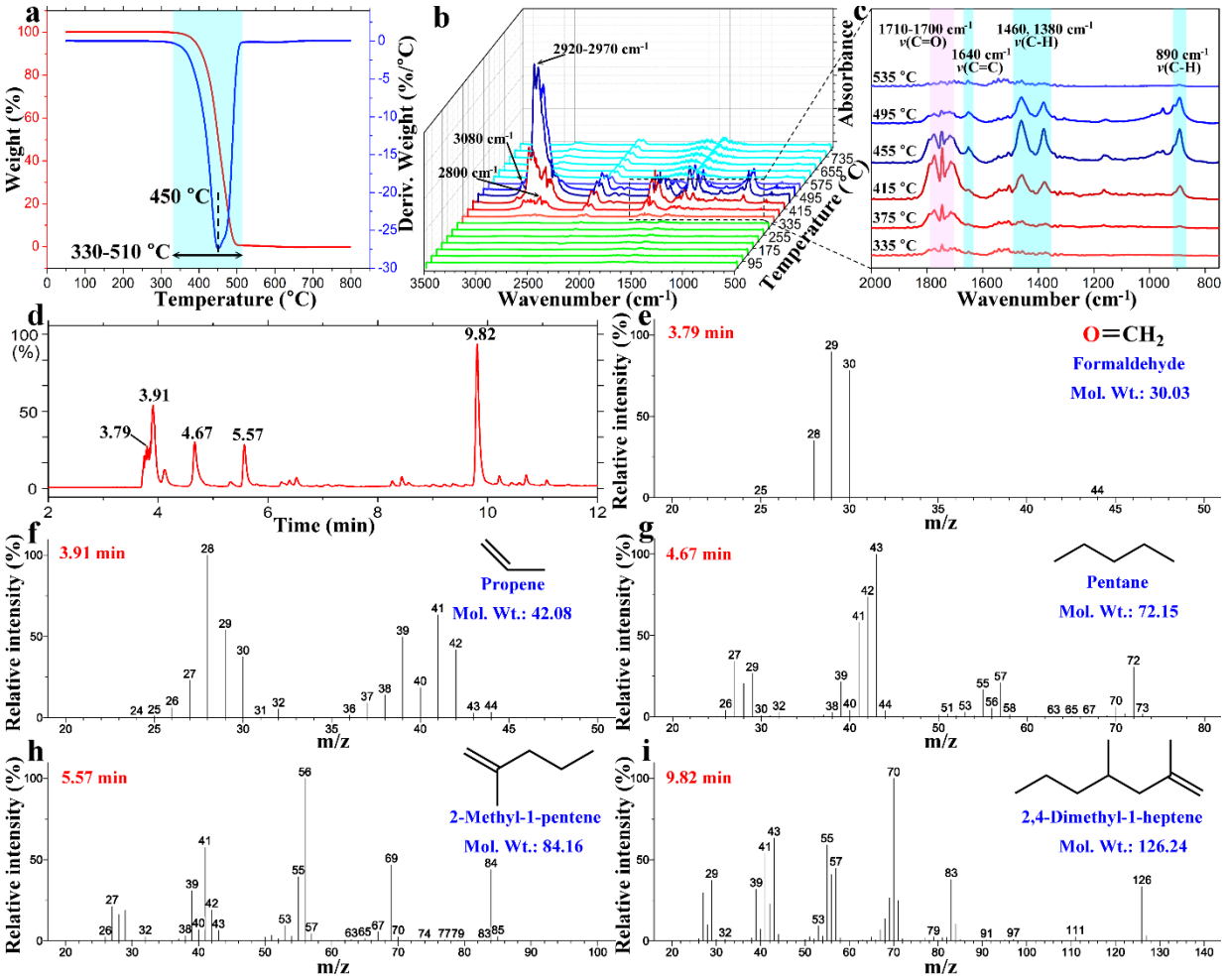

Figure S18. TG-FTIR-GC-MS analysis of PP doped with PR and CuNWs@POM core-shell microfibers. (a) TG and DTG curves of the sample from 50 °C to 800 °C at 100 °C/min in N_2 atmosphere. **(b, c)** The in-situ FTIR spectroscopy for detecting evolved gaseous products during the thermal decomposition of the sample from 50 to 800 °C. **(d)** The gas chromatography (GC) spectrum of thermal decomposition products of the sample at 430 °C. Mass spectrum (MS) to identify the thermal decomposition products, formaldehyde **(e)**, propene **(f)**, pentane **(g)**, 2-methyl-1-pentene **(h)**, and 2,4-dimethyl-1-heptene **(i)**.

Figure S18 is the TGA-FTIR-GC-MS analysis of PP doped with PR and CuNWs@POM core-shell microfibers. **Figure S18**a is the TG and TGA curves of the sample. The sample was heated from 50 °C to 800 °C in N_2 atmosphere with a 100 °C/min heating rate. Herein, it is worth noting that the heating rate in the TG experiment was set at 100 °C/min to simulate the situation of the instantaneous high temperature generated during LDW as much as possible. As shown in **Figure S18**a, the decomposition temperature of PP doped with PR and CuNWs@POM core-shell microfibers is at 330-510 °C, and the maximum weight loss temperature is at 450 °C. The in-situ FTIR spectroscopy for detecting gaseous products evolved from TGA during thermal

decomposition of polymers was performed from 50 to 800 °C. In **Figure S18**b, no gaseous compounds are detected by FTIR before 330 °C because the polymers have not decomposed yet (green curves). The recorded spectra show strong functional group peaks at the decomposition temperature of 330-510 °C (red and blue curves). The 3080 and 2920-2970 cm^{-1} peaks are related to C−H stretching in unsaturated and saturated carbons, respectively. The peak at 2800 cm^{-1} is assigned to C−H stretching in the aldehyde group. In the magnified **Figure S18**c, the characteristic peaks of C=O are recorded at 1710-1700 cm^{-1}, indicating the formation of aldehydes. And the peak at 1640 cm^{-1} is attributed to C=C stretching. The C−H bending of CH_2, CH_3, and $-CH=CH_2$ are observed at 1460, 1380, and 890 cm^{-1}, respectively, demonstrating that hydrocarbons are formed. The results of in-situ FTIR spectroscopy show that the gaseous products of polymers' thermal decomposition consist of aldehydes and hydrocarbons. More importantly, the production sequence of these gaseous small molecule compounds can also be detected from in-situ FTIR spectroscopy. As shown in **Figure S18**b, c, the characteristic peaks of aldehydes appear at 335 °C, reaching a maximum at 415 °C and gradually weakening. In contrast, the characteristic peaks of hydrocarbons arise at 415 °C, reaching a maximum at 455 °C and disappearing at 535 °C. The results indicate that the initial decomposition products of the polymer at high temperatures are formaldehyde gas, followed by hydrocarbon gas. As is known to all, the high-temperature thermal decomposition products of polyformaldehyde (POM) are formaldehyde, while that of low-density polyethylene (LDPE) and polypropylene (PP) are hydrocarbons. That is to say, the thermal decomposition of POM occurred first, followed by LDPE and PP during the rapid temperature rise.

To further identify these pyrolysis products, including the molecular weight and chemical structure of gaseous organic compounds, the GC-MS was conducted at 430 °C. **Figure S18**d presents the gas chromatography (GC) result of PP doped with PR and CuNWs@POM core-shell microfibers during the TGA-FTIR-GC-MS test. It can be observed that there are five main peaks with retention times of 3.79 min, 3.91 min, 4.67 min, 5.57 min, and 9.82 min. Obviously,

the peak intensity at 9.82 min is the strongest. The corresponding mass spectra (MS) of these five peaks are provided in **Figure S18**e-i. According to the matching results of the MS database, the thermal decomposition product at 3.79 min is formaldehyde. And the pyrolysis products at 3.91 min, 4.67 min, 5.57 min, and 9.82 min are propene, pentane, 2-methyl-1-pentene, and 2,4-mimethyl-1-heptene, respectively. The results successfully reveal that the thermal decomposition products of the PP doped with CuNWs@POM core-shell microfibers are formaldehyde and hydrocarbons mixture.

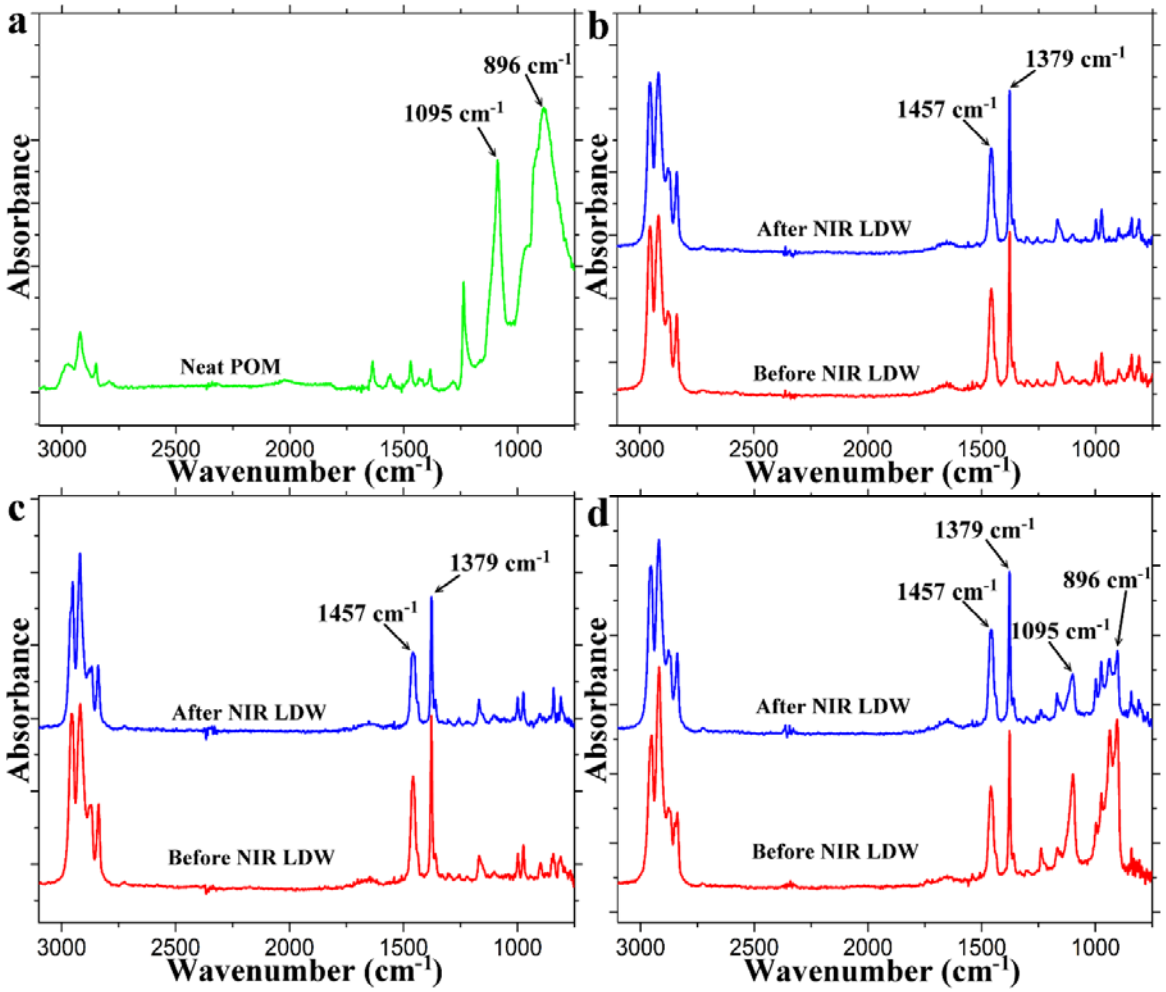

Figure S19. ATR-FTIR spectroscopy of samples. (a) ATR-FTIR spectrum of POM. ATR-FTIR spectra of neat PP **(b)**, PP doped with PR and CuNWs **(c)**, and PP doped with PR and CuNWs@POM core-shell microfibers **(d)** before and after NIR LDW.

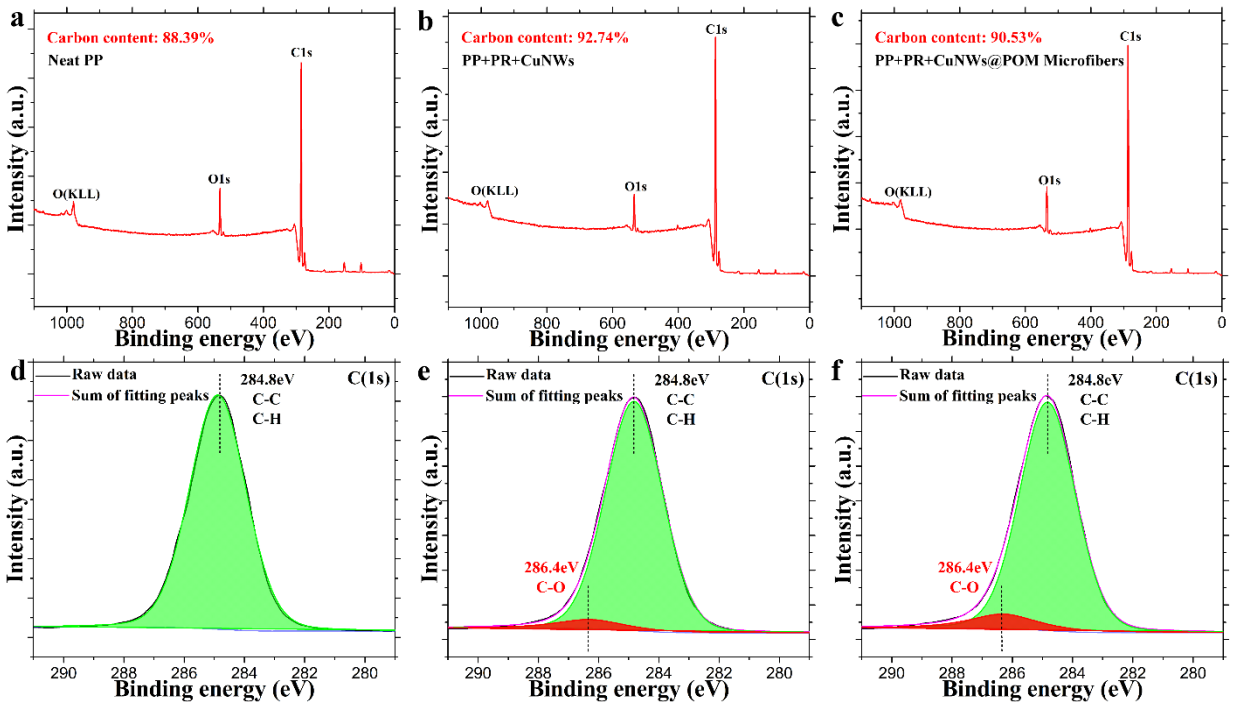

Figure S20. XPS analysis of samples. Surface XPS spectra of neat PP **(a)**, PP doped with PR and CuNWs **(b)**, and PP doped with PR and CuNWs@POM core-shell microfibers **(c)** after NIR LDW. High-resolution C 1s XPS spectra of neat PP **(d)**, PP doped with PR and CuNWs **(e)**, and PP doped with PR and CuNWs@POM core-shell microfibers **(f)** after NIR LDW.

In addition, the XPS analyses further confirm the difference in the degree of carbonization (**Figure S20**a-c). After NIR LDW, the carbon contents of neat PP, PP doped with PR and CuNWs, and PP doped with PR and CuNWs@POM core-shell microfibers are 88.39, 92.74, and 90.53%, respectively. It can be observed that the carbonization degree of PP doped with PR and CuNWs@POM core-shell microfibers is significantly lower than PP doped with PR and CuNWs. In fact, the results of DSC in **Figure 4**i have demonstrated that POM can be decomposed entirely at high temperatures. During NIR LDW, CuNWs absorb the laser energy and generate heat to decompose the POM, and the decomposition of POM will absorb a certain amount of heat. At the same time, the gas produced will take away the heat, causing a relatively low temperature. It also explains why the surface temperature recorded on the PP doped with PR and CuNWs@POM core-shell microfibers is lower than the PP doped with PR and CuNWs during NIR LDW (**Figure S17**e, f). Thus, the carbonization degree in the white pattern is significantly lower than in the gray-black pattern at a relatively low temperature.

And corresponding high-resolution C 1s XPS curve fitting results were conducted by the asymmetric Lorentzian-Gaussian sum function (**Figure S20**d-f). Compared with only the main C 1s peak of neat PP appearing at 284.8 eV, which is assigned to C−C/C−H groups (**Figure S20**d), another new C 1s peak at 286.4 eV attributed to −C−O groups is observed in the PP doped with PR and CuNWs, and PP doped with PR and CuNWs@POM core-shell microfibers (**Figure S20**e, f).[5] And the relative molar contents of carbon elements contributed from C−C/C−H and C−O groups are shown in **Table S1**. The contents of −C−O groups for neat PP, PP doped with PR and CuNWs, and PP doped with PR and CuNWs@POM core-shell microfibers are 0, 6.09, and 8.21%, respectively. The generation of the −C−O groups is due to the thermal oxidation of polymer during NIR LDW. Here, the content of −C−O groups in PP doped with PR and CuNWs@POM core-shell microfibers is higher than that of PP doped with PR and CuNWs because there is still some undecomposed POM (containing −C−O groups) on the polymer surface after LDW.

Table S1. Relative molar content of the carbon element from C−C/C−H and C−O. It is calculated based on the area of the fitted peaks at 284.8 eV (C–C/C–H) and 286.4 eV (C–O) in **Figure S20.**

Samples	The C element from C−O, 286.4 eV (mol%)	The C element from C−C/C−H, 284.8 eV (mol%)
Neat PP	0.00	100.00
PP doped with neat CuNWs	6.09	93.91
PP doped with CuNWs@POM microfibers	8.21	91.79

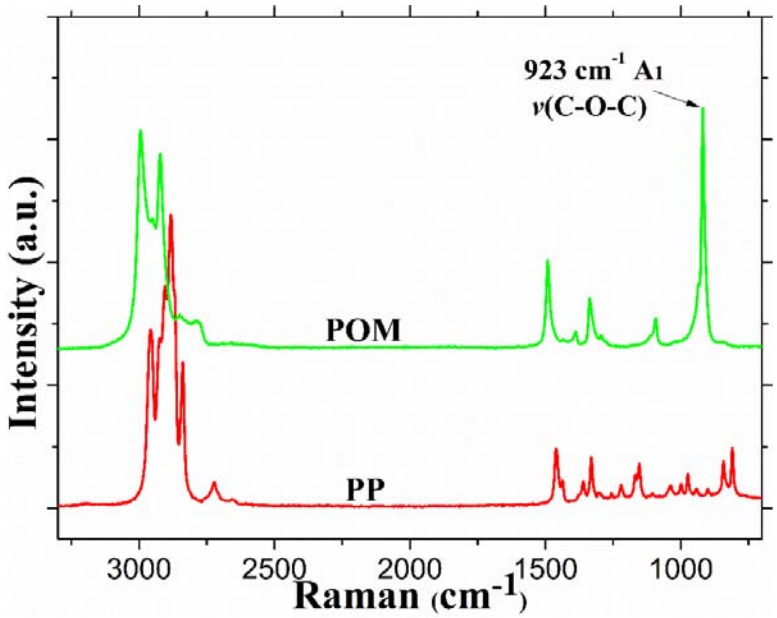

Figure S21. Surface micro-Raman spectra of the neat PP and POM.

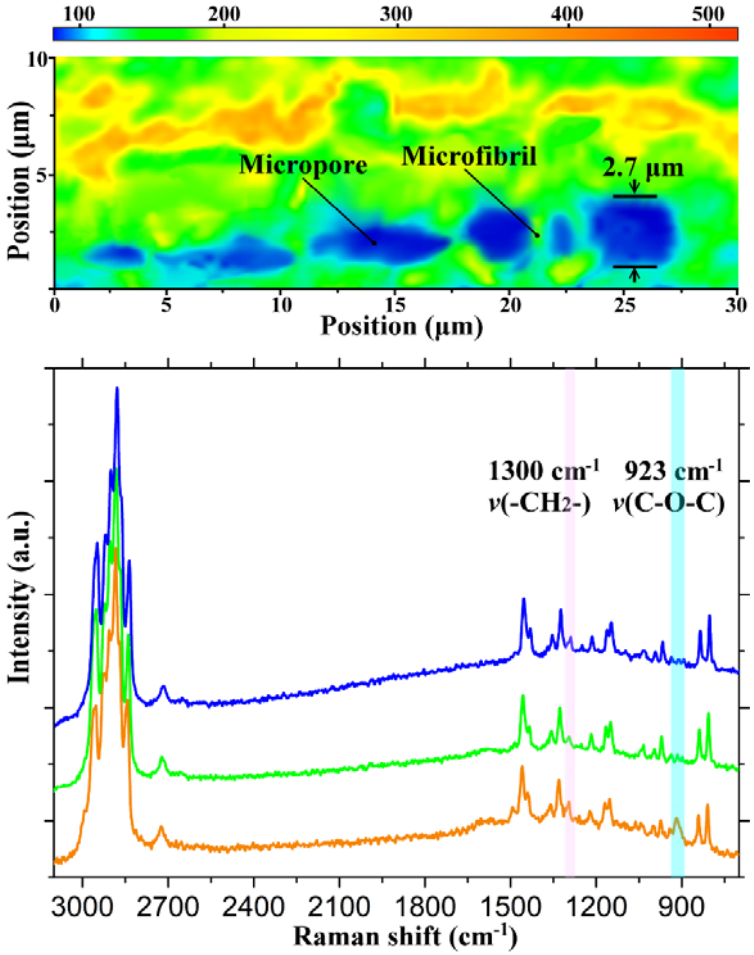

Figure S22. The cross-sectional Raman imaging of the craze-like microstructure and corresponding Raman spectra at blue, green, and brown regions.

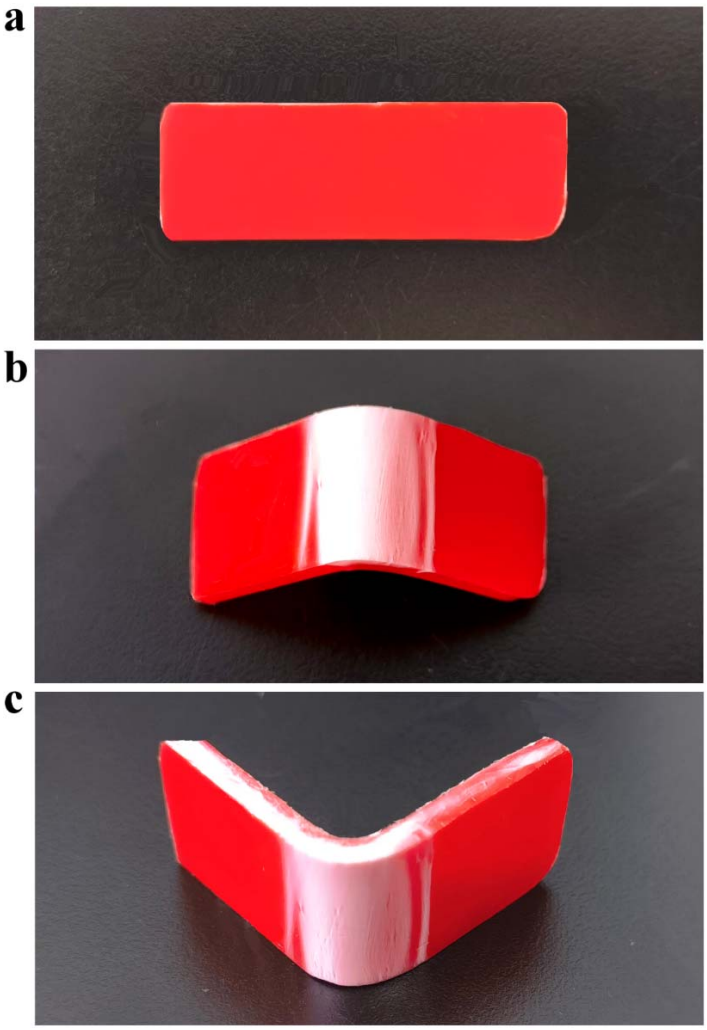

Figure S23. Digital photographs of PP doped with PR and CuNWs@POM core-shell microfibers before (a) and after bent by the external force (b, c).

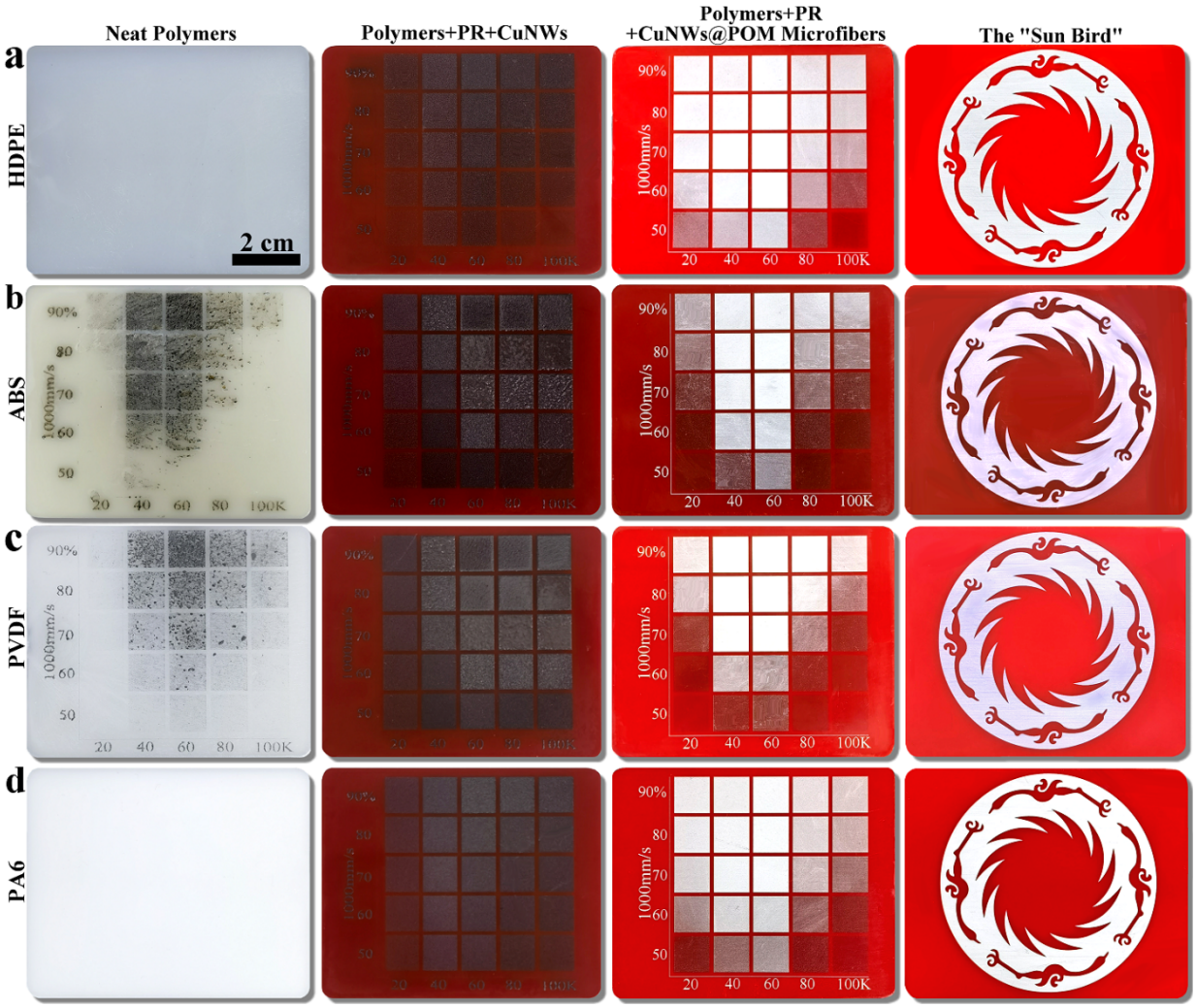

Figure S24. Digital photographs of white structural color patterns prepared by NIR LDW on general-purpose polymers. (a) High-density polyethylene (HDPE). **(b)** Acrylonitrile-butadiene-styrene copolymers (ABS). **(c)** Polyvinylidene fluoride (PVDF). **(d)** Polyamide 6 (PA6). For the 1064 nm NIR laser, the pulse frequency, laser power, and scanning speed are 60 kHz, 16 W, and 1000 mm/s, respectively.

Figure S24 presents the photographs of prepared neat polymers (HDPE, ABS, PVDF, and PA6), polymers (HDPE, ABS, PVDF, and PA6) doped with 0.05 wt% PR and 0.021 wt% CuNWs, and polymers (HDPE, ABS, PVDF, and PA6) doped with 0.05 wt% PR and 7 wt% CuNWs@POM core-shell microfibers after NIR LDW.

As shown in **Figure S24**, the neat HDPE and PA6 show no color change after NIR LDW because of no absorption to 1064nm NIR laser. For neat ABS and PVDF, the color change phenomenon appears on the surface after LDW, but the black square patterns are blurry, probably due to the presence of a small number of impurities absorbing the NIR laser in the two polymers.

In contrast, polymers (HDPE, ABS, PVDF, and PA6) doped with PR and CuNWs all show a strong color change after laser irradiation, resulting in black and dark gray square patterns on the red matrix because CuNWs have a high absorption of NIR laser. However, the gray-black patterns on these polymers doped with PR and CuNWs are very rough, especially for ABS and PVDF doped with PR and CuNWs. Surprisingly, polymers (HDPE, ABS, PVDF, and PA6) doped with CuNWs@POM core-shell microfibers all present an obvious white structural color after NIR LDW. The high contrast and high-resolution white square patterns are clearly prepared on the sample's surface. Furthermore, the laser parameter at (16 W, 60 kHz, and 1000 mm/s,) was chosen to prepare the "Sun Bird" white structural color patterns. As expected, the white "Sun Bird" patterns with high contrast and sharpness are also fabricated by LDW in these polymers, exhibiting a broad application prospect of preparing white structural color in CuNWs@POM core-shell microfibers-based polymers.

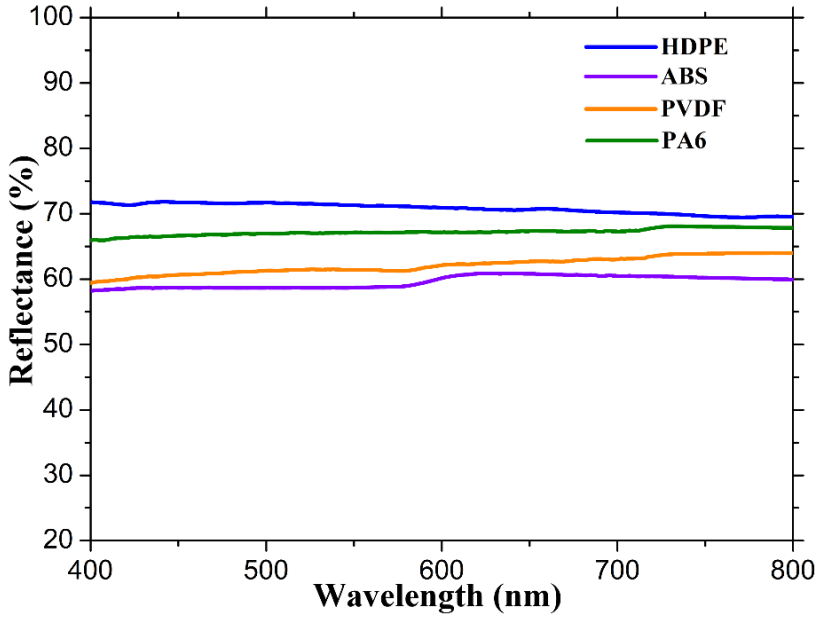

Figure S25. Reflectance of polymers (HDPE, ABS, PVDF, and PA6) doped with CuNWs@POM core-shell microfibers after LDW.

Figure S26. Digital photographs of laser-written white structural color samples taken at four oblique angles (0°, 30°, 60°, and 80°). Herein, the thickness of the polymer plates is 3 mm.

Figure S27. Digital photographs of the white patterns placed for 18 months at ambient conditions. (a) PP doped with red dyes and CuNWs@POM core-shell microfibers. **(b)** PP doped with blue dyes and CuNWs@POM core-shell microfibers. **(c)** PP doped with green dyes and CuNWs@POM core-shell microfibers. **(d)** PP doped with magenta dyes and CuNWs@POM core-shell microfibers. The white structural color patterns are prepared by NIR LDW with the pulse frequency, laser power, and scanning speed of 60 kHz, 16 W, and 1000 mm/s, respectively.

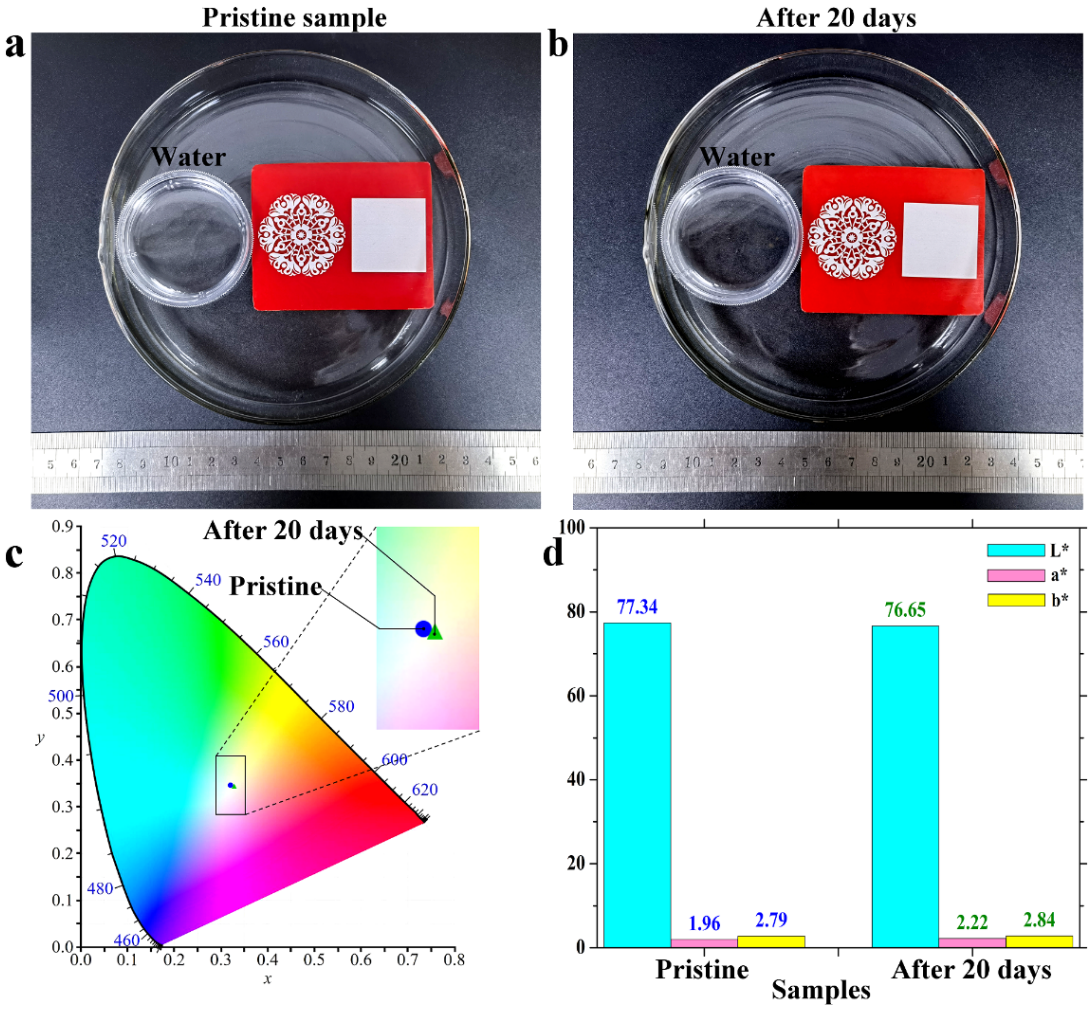

Figure S28. Color stabilization tests in harsh environments. (a, b) Digital photographs of the pristine sample after LDW and tested sample after 20 days in high humidity and high-temperature environments. **(c)** CIE chromaticity diagram of the white pattern before and after the color stability tests. **(d)** Measured raw data of the pristine sample and the test sample, including values of L*, a*, and b*. The average L*, a*, and b* values were obtained by measuring the surface of the same sample 5 times at different positions.

Herein, we conducted additional color stabilization experiments in harsh environments. To mimic the harsh environment in practical applications, the polymer plates after LDW were placed in a closed container containing approximately 30 mL of water. Then, the device was put in an oven at 60 °C for 20 days. **Figure S28**a, b are the photographs of the pristine sample after LDW and the tested sample after 20 days in high humidity and high-temperature environments. After being exposed to these extreme environments for 20 days, the white structural color pattern

still has high contrast and high resolution, and the surface of the white pattern is still very flat (**Figure S28**b).

The color fastness tests were performed based on the color difference (ΔE) measurement of an identical sample before and after the color stability tests. According to "CIE 1931" standards, ΔE represents the color difference between the pristine and test samples. Every color coordinate corresponds to a group of L*a*b* values, and ΔL*, Δa*, and Δb* represent the differences in lightness, red-green, and yellow-blue differences, respectively. L_0, a_0, and b_0 represent the measured values of the pristine sample.

The color difference (ΔE) was calculated using the following formula:

$$\Delta E^* = \sqrt{(\Delta L^*)^2 + (\Delta a^*)^2 + (\Delta b^*)^2}$$

$$\Delta L^* = L^* - L_0$$

$$\Delta a^* = a^* - a_0$$

$$\Delta b^* = b^* - b_0$$

The CIE chromaticity diagram illustrates the color change of the white pattern before and after the color stability tests (**Figure S28**c). One can see that there is only a very slight shift in the CIE coordinates after 20 days in high-humidity and high-temperature environments. **Figure S28**d is the measured raw data of the pristine sample and the test sample, including values of L*, a*, and b*, proving that the color change is tiny. Furthermore, the color difference (ΔE) was calculated at 0.74. Human eyes can barely distinguish the difference between the test and pristine samples when ΔE* is below 1.0. The above results indicate that the white structural color is stable in harsh environments.

The high color stability is because polypropylene contains many methyl groups, which are non-polar groups. So, polypropylene is a hydrophobic material. More importantly, the white structural color pattern after LDW has uniform micro-bulge structures, further enhancing the polymer surface's hydrophobicity (**Figure S16**). In addition, the high-temperature environment

of 60 °C will not destroy the craze-like microfibers in polymer because the melting temperature of the polymer is high enough (the melting temperature of PP exceeds 160 °C). In fact, the white structural color on polymers cannot change until the polymers are recycled. Therefore, this white structural color possesses excellent stability and weather resistance even in harsh environments.

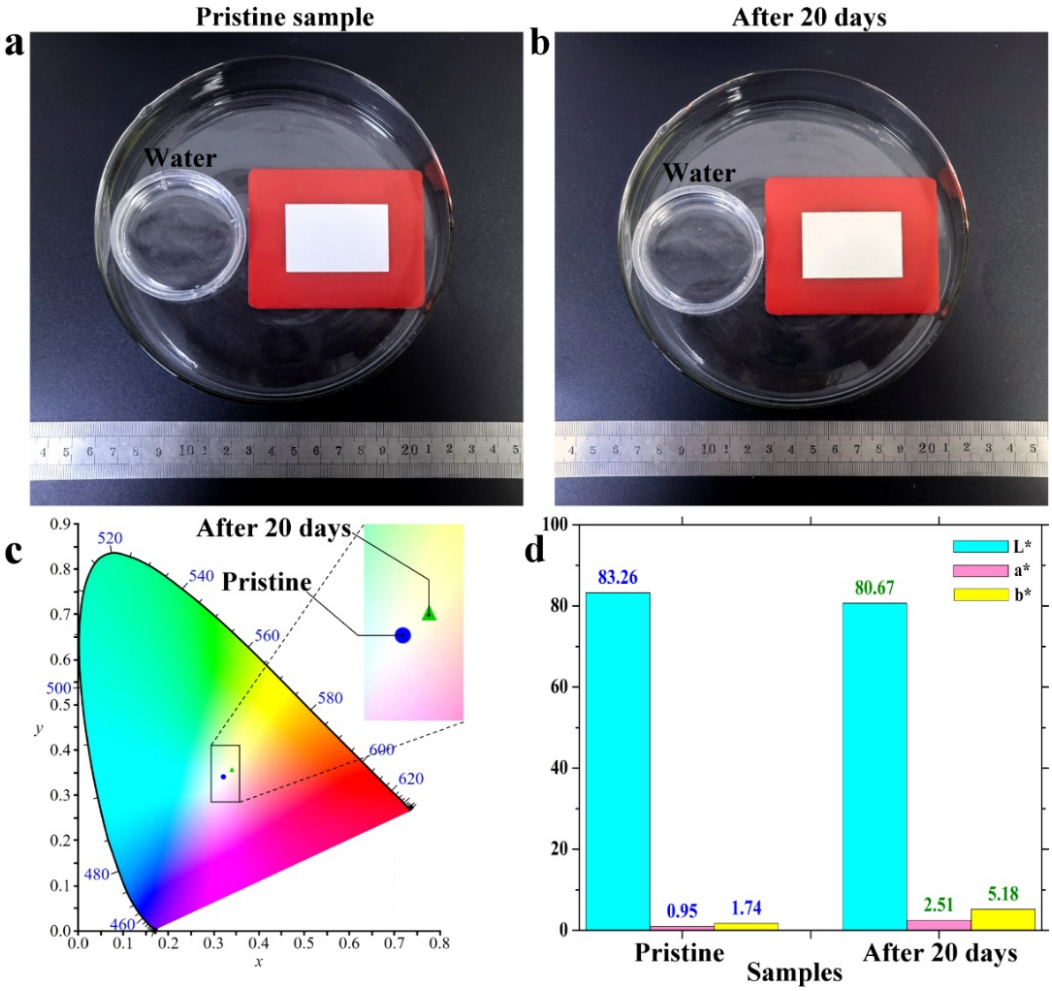

Figure S29. Color stability tests in harsh environments. (a, b) Digital photographs of the pristine sample after spray painting and tested sample after 20 days in high humidity and high temperature environments. **(c)** CIE chromaticity diagram of the white pattern before and after the color stability tests. **(d)** Measured raw data of the pristine sample and the test sample, including values of L*, a*, and b*. The average L*, a*, and b* values were obtained by measuring the surface of the same sample 5 times at different positions.

To compare laser direct writing white structural color with conventional white pigments or dyes in the same harsh environments, we purchased commercial white paints for the white coloration of polymer surfaces. The commercial white paints consist of white pigments, resins, fillers, solvents, and additives. Herein, a spraying process was used to color the polymer surface. Firstly,

the surface of the PP plate was cleaned before spraying to improve the surface adhesion. Then, a rectangular hollow PET mask was attached to the surface of the PP plate. The spraying process was carried out on the PP surface with a certain spraying distance and speed. Finally, after natural drying for 48 hours, a white rectangular pattern (45mm×30mm) was fabricated on the polymer surface. The polymer plate, after spray painting, was placed in a closed container containing approximately 30 mL of water, and the device was put in an oven at 60 °C for 20 days. The color change after the color stability tests is represented by a chromaticity diagram according to the "CIE 1931" standards.

Figure S29a, b are the photographs of the pristine sample after spray painting and the tested sample after 20 days in high-humidity and high-temperature environments, respectively. After spray painting, the rectangular pattern shows a bright white color (**Figure S29**a). However, after being exposed to extreme environments for 20 days, the white pattern prepared by spray painting is slightly darkened and exhibits a yellowing phenomenon (**Figure S29**b). The color change is probably ascribed to the poor stability and weather resistance of the chemicals added to the paint. Compared with the white pattern prepared by spray painting, the white structural color pattern produced by LDW shows almost no color change in the same extreme environment (**Figure S28**a, b). In addition, the CIE chromaticity diagram illustrates the color change of the white pattern before and after the color stability tests. It can be observed that the CIE coordinates move from the white region to the light-yellow region after being placed in high-humidity and high-temperature environments for 20 days (**Figure S29c**). **Figure S29d** is the measured raw data of the pristine sample and the test sample, including values of L*, a*, and b*. As shown in **Figure S29**d, for the white pattern prepared by spray painting, the L* value decreases from 83.26 to 80.67, demonstrating a decrease in the brightness of the white pattern after the color stability tests. The a* value changes from 0.95 to 2.51, and the b* value changes from 1.74 to 5.18, indicating a yellowing phenomenon. In harsh environments, the white color produced by spray painting is more vivid (L*=80.67, a*=2.51, and b*=5.18), but the white structural color prepared

by LDW is purer (L*=76.65, a*=2.22, and b*=2.84). Besides, the color difference (ΔE) of white color produced by spray painting (white pigments) is calculated at 4.58, which is significantly higher than that of white structural color prepared by LDW (0.74).

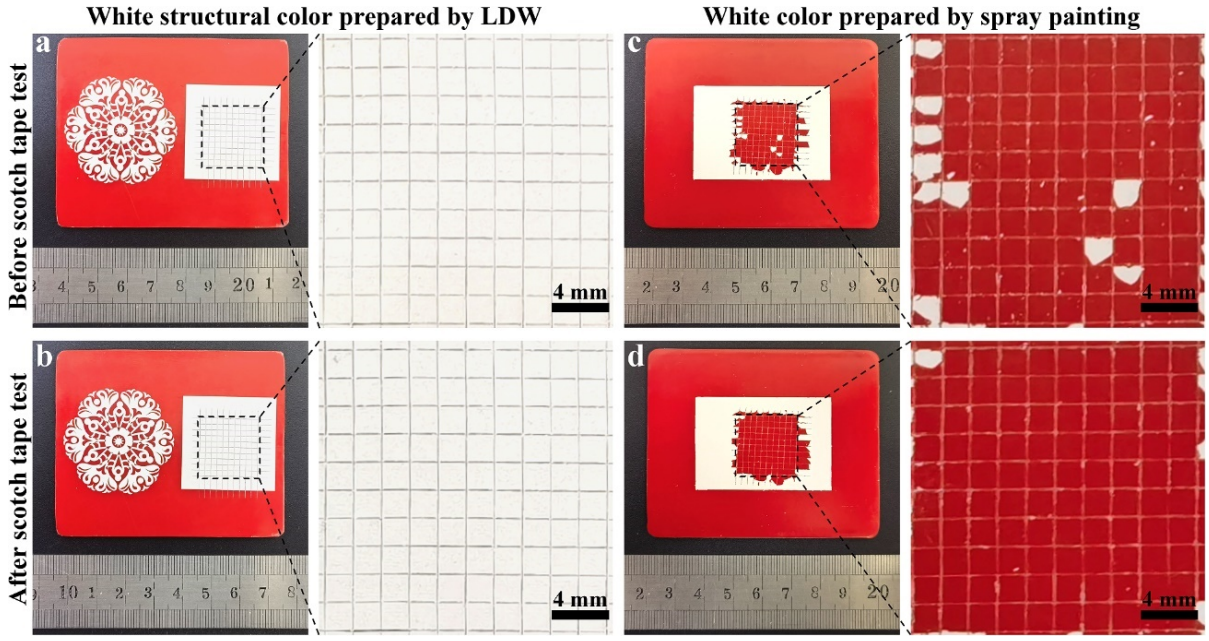

Figure S30. Adhesion test of samples after being exposed to harsh environments for 20 days. **(a, b)** Digital photographs of the white structural color pattern prepared by LDW before and after scotch tape tests. **(c, d)** Digital photographs of the white color pattern produced by spray painting before and after scotch tape tests.

In addition, we tested the adhesion strength of these white color layers on the polymer surface using a standard cross-cut tape test (ASTM D3359). As shown in **Figure S30**a, b, after being exposed to harsh environments for 20 days, the white structural color layer produced by LDW still reaches the highest level of 5B, which completely meets the needs for practical applications. In comparison, for the white color layer prepared by spray painting, most of the white area was removed before the scotch tape test, showing the lowest level of 0B after the scotch tape test (**Figure S30**c, d). In fact, the adhesion between paints (or inks) and polymers is inherently poor (especially for non-polar polymers such as PP), and its adhesion will be further decreased in high-humidity and high-temperature environments. The results indicate that the white structural color layer by LDW possesses excellent adhesion properties even in harsh environments for 20

days, while the white color layer prepared by spray painting has extremely poor adhesion properties under the same environment.

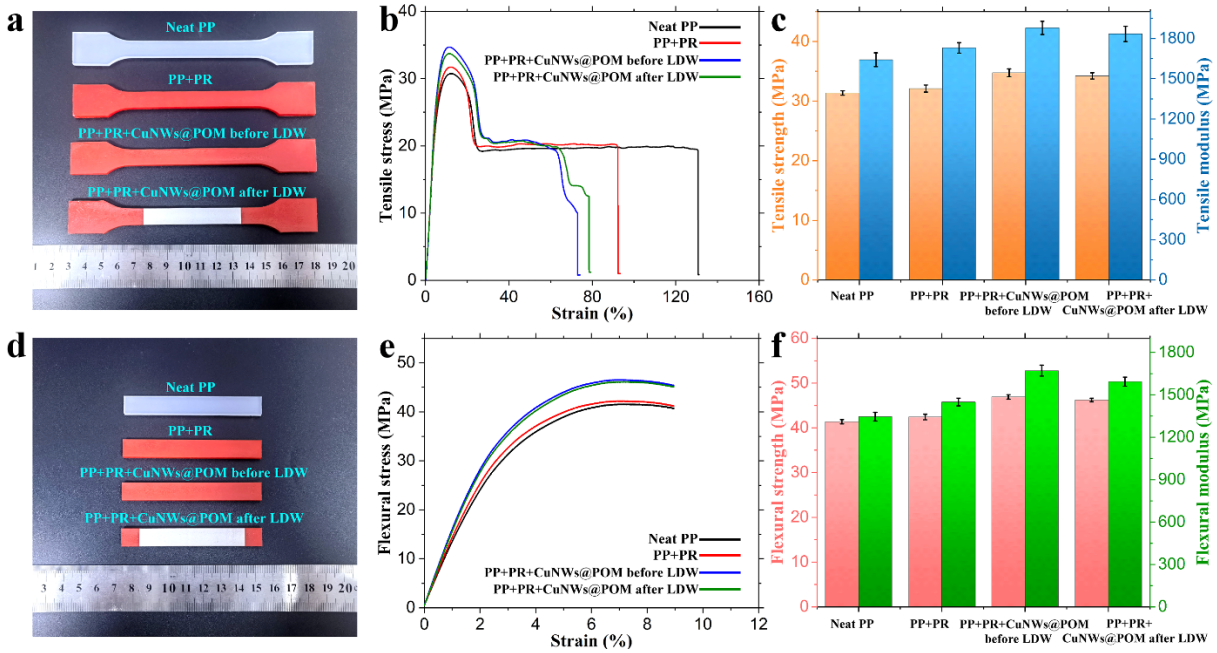

Figure S31. Mechanical properties of neat PP, PP doped with PR, and PP doped PR and CuNWs@POM core-shell microfibers before and after LDW. (a) Photographs of the dumbbell-shaped tensile specimens. **(b)** Representative tensile stress-strain curves of samples. **(c)** Tensile strength and modulus values calculated from the tensile stress-strain curves. **(d)** Photographs of the flexural specimens. **(e)** Representative flexural stress-strain curves of samples. **(f)** Flexural strength and modulus values calculated from the flexural stress-strain curves.

Table S2. Mechanical properties of neat PP, PP doped with PR, and PP doped PR and CuNWs@POM core-shell microfibers before and after LDW obtained from Figure S31.

Samples	Tensile strength (MPa)	Tensile modulus (MPa)	Flexural strength (MPa)	Flexural modulus (MPa)
Neat PP	31.4	1641.5	41.4	1345.2
PP+PR	32.1	1729.4	42.4	1449.0
PP+PR+CuNWs@POM core-shell microfibers before LDW	34.7	1878.8	46.90	1671.2
PP+PR+CuNWs@POM core-shell microfibers after LDW	34.2	1833.9	46.2	1592.6

As shown in **Figure S31 and Table S2**, it can be observed that the tensile strength, tensile modulus, flexural strength, and flexural modulus of PP/PR composites are higher than those of neat PP. This indicates that the addition of PR positively affects the mechanical properties of PP. Surprisingly, the tensile strength, tensile modulus, flexural strength, and flexural modulus all increase significantly with the addition of CuNWs@POM core-shell microfibers. The mechanical properties of PP/PR/CuNWs@POM core-shell microfiber composites are reinforced compared to neat PP and PP/PR. The enhanced mechanical properties are because of the embedding of CuNWs@POM core-shell microfibers with high strength and modulus in the PP matrix. In our work, the addition of CuNWs@POM core-shell microfibers in the PP matrix not only plays a key role in laser-induced craze-like microstructures but also probably serves as fillers to enhance the mechanical properties of PP. In addition, compared to before LDW, the mechanical properties of PP/PR/CuNWs@POM core-shell microfibers after LDW remain almost equivalent. This demonstrates that the craze-like microstructures generated in the polymer after LDW have no negative effect on the mechanical properties of PP/PR/CuNWs@POM core-shell microfiber composites.

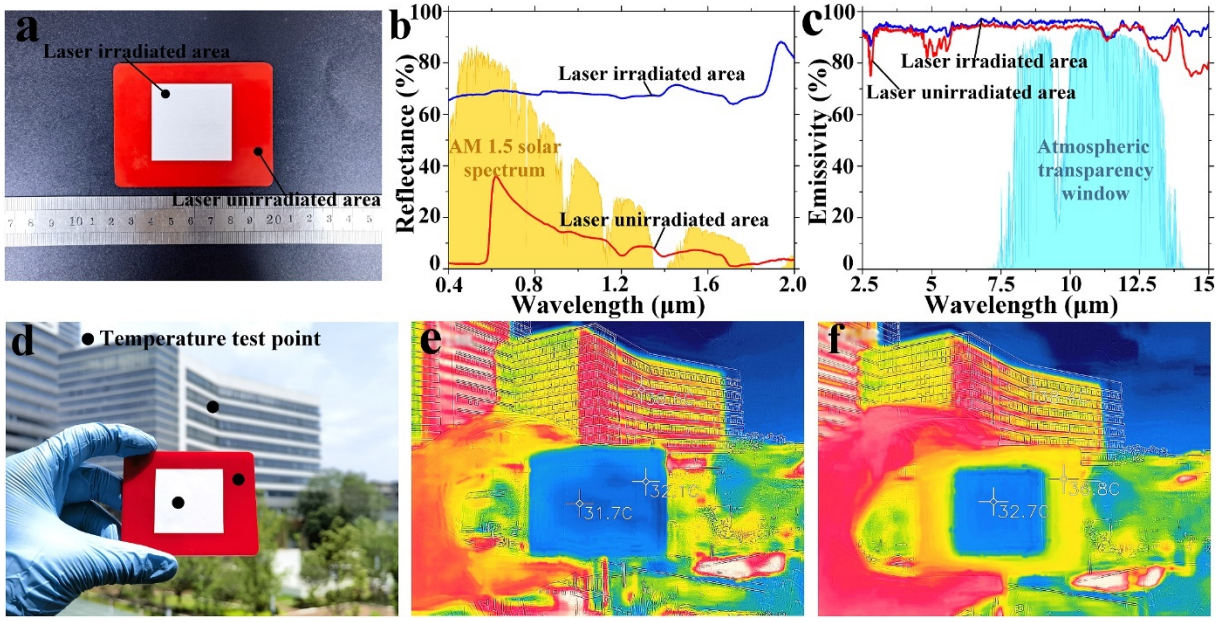

Figure S32. Optical properties and outdoor cooling test of the passive radiative cooling materials. (a) Digital photograph of passive radiative cooler prepared by LDW (40 mm × 40 mm). **(b)** Spectral Reflectance of the laser-irradiated and unirradiated areas in the solar waveband (0.4-2 μm) against AM 1.5 solar spectrum. **(c)** Spectral emissivity of the laser-irradiated and unirradiated areas in the mid-infrared region (2.5-15 μm) against atmospheric transparency window. **(d)** Digital photograph of the prepared passive cooler outdoors (on August 10, 2023, a sunny day with an ambient temperature of 31 °C). **(e)** IR image when the polymer plate was initially exposed to sunlight (2023/08/10 12:00). **(f)** IR image when the polymer plate was exposed to sunlight after 1.5 h (2023/08/10 13:30).

As is shown in **Figure S32**a, a larger white structural color pattern (40 mm × 40 mm) was prepared on polymer by LDW for the following tests. In order to study the solar light reflection ability of the laser-irradiated and unirradiated areas, we collected its solar reflectance spectra from 0.4 μm to 2 μm. In **Figure S32**b, compared with the laser unirradiated area (red curve), the laser irradiated area (white structural color pattern prepared by laser direct writing craze-like microstructures) shows an apparent broadband reflection in the solar waveband (blue curve). With the introduction of the craze-like microstructures, the white structural color area exhibits obvious improvement in solar reflection. As shown in **Figure S32**c, it can be observed that both the laser-unirradiated area and laser-irradiated area (laser direct writing craze-like microstructures) show strong thermal emission in the mid-infrared region. The measured emissivity spectra also demonstrate that in the atmospheric transparency window (8-13 μm), the

laser-irradiated area has an average emissivity of ~94% (blue curve), slightly higher than the laser-unirradiated area (~92%) (red curve). The results indicate that laser direct writing craze-like microstructures can not only significantly increase the reflectance of polymer surfaces within the solar spectrum range, but also slightly enhance the emissivity in the atmospheric transparency window.

The high reflectance in the solar spectrum range and high emissivity of ~94% in the atmospheric transparency window (8 to 13 mm) can enhance the cooling performance of the white structural color pattern. To reveal its cooling capability, an outdoor test was conducted (Chengdu, China). Herein, the surface temperature of the polymer plate was recorded by an IR camera. **Figure S32**d is a digital photograph of the prepared passive cooler outdoors (on August 10, 2023, a sunny day with an ambient temperature of 31 °C). The laser-irradiated area on the passive cooler presents a bright white structural color. **Figure S32**e is an IR photograph taken quickly when the polymer plate was initially exposed to sunlight. One can see that the temperature in laser irradiated area (31.7 °C) is only 0.4 °C lower than that of the laser unirradiated area (32.1 °C) at this time (2023/08/10 12:00). Surprisingly, as shown in **Figure S32**f, the surface temperature of laser irradiated area (32.7 °C) is significantly lower than that of laser unirradiated area (36.8 °C) after reaching stable state under direct sunlight illumination (2023/08/10 13:30), decreasing 4.1 °C. In comparison, the surface temperature of the building reaches 38.6 °C. The results demonstrate that the cooling performance of the passive radiative cooling structure is excellent.

3. Description of Supplementary Movies:

Movie S1: The preparation of the white structural color pattern "Sun Bird" on PP doped with PR and CuNWs@POM core-shell microfibers by 1064 nm NIR laser direct writing. The laser power, pulse frequency, and scanning speed are 16 W, 60 kHz, and 1000 mm/s, respectively.

Movie S2: The preparation comparison of the black pattern on PP doped with PR and CuNWs and white structural color pattern on PP doped with PR and CuNWs@POM core-shell microfibers by 1064 nm NIR laser direct writing. The laser power, pulse frequency, and scanning speed are 16 W, 60 kHz, and 1000 mm/s, respectively.

Movie S3: Practical applications of polymer white structural color: fabricating patterns in traffic signs, supermarket labels, color keyboards, and garbage sorting signs by laser direct writing. The laser power, pulse frequency, and scanning speed are 16 W, 60 kHz, and 1000 mm/s, respectively.

Movie S4: The corresponding real-time thermal imaging video of **Movie S1**. The laser power, pulse frequency, and scanning speed are 16 W, 60 kHz, and 1000 mm/s, respectively. We can observe a significant temperature rise at the positions during 1064 nm NIR laser direct writing.

4. References

1. L. Xu, Y. Yang, Z. W. Hu and S. H. Yu, *ACS Nano*, 2016, **10**, 3823-3834.
2. Z. Fan, B. Liu, Z. Li, L. Ma, J. Wang and S. Yang, *RSC Advances*, 2014, **4**, 23319.
3. J. Feng, R. Xu, J. Zhang, Z. Zheng and T. Zhou, *ACS Appl. Mater. Interfaces*, 2022, **14**, 14817-14833.
4. L. Wen, T. Zhou, J. Zhang and A. Zhang, *ACS Appl. Mater. Interfaces*, 2016, **8**, 28077-28085.
5. A. Rjeb, S. Letarte, L. Tajounte, M. C. El Idrissi, A. Adnot, D. Roy, Y. Claire and J. Kaloustian, *J. Electron Spectrosc.* 2000, **107**, 221.